Laurila, E.; Roenby, J.; Maakala, V.; Peltonen, P.; Kahila, H.; Vuorinen, V.

Analysis of viscous fluid flow in a pressure-swirl atomizer using large-eddy simulation

Published in:
International Journal of Multiphase Flow

DOI:
10.1016/j.ijmultiphaseflow.2018.10.008

Published: 01/04/2019

Document Version
Peer-reviewed accepted author manuscript, also known as Final accepted manuscript or Post-print

Please cite the original version:
Laurila, E., Roenby, J., Maakala, V., Peltonen, P., Kahila, H., & Vuorinen, V. (2019). Analysis of viscous fluid flow in a pressure-swirl atomizer using large-eddy simulation. *International Journal of Multiphase Flow*, *113*, 371-388. https://doi.org/10.1016/j.ijmultiphaseflow.2018.10.008

Analysis of viscous fluid flow in a pressure-swirl atomizer using large-eddy simulation

E. Laurila[a,*], J. Roenby[b], V. Maakala[c], P. Peltonen[a], H. Kahila[a], V. Vuorinen[a]

[a] *Department of Mechanical Engineering, Aalto University School of Engineering,*
Puumiehenkuja 5 02150 Espoo, Finland
[b] *Department of Mathematical Sciences, Aalborg University, Frederikskaj 10A 2450*
København SV, Denmark
[c] *Andritz, Tammasaarenkatu 1 00180 Helsinki, Finland*

Abstract

A computational fluid dynamics study is carried out on the inner nozzle flow and onset of liquid sheet instability in a large-scale pressure-swirl atomizer with asymmetric inflow configuration for high viscosity fluids. Large-eddy simulations (LES) of the two-phase flow indicate the unsteady flow character inside the nozzle and its influence on liquid sheet formation. A novel geometric volume-of-fluid (VOF) method by Roenby et al., termed `isoAdvector`, is applied for sharp interface capturing (Roenby J., Bredmose H., Jasak H., 2016, A computational method for sharp interface advection, Royal Society Open Science 3). We carry out a Reynolds number sweep ($420 \leq Re \leq 5300$) in order to investigate the link between the asymmetric inner nozzle flow and liquid sheet characteristics in laminar, transitional and fully turbulent conditions. Inside the nozzle, the numerical simulations reveal counter-rotating Dean vortices, flow impingement locations, and strong asymmetric flow features at all investigated Reynolds numbers. A helical, rotating gaseous core is observed when $Re \geq 1660$. For laminar flow ($Re = 420$), an S-shaped liquid film is observed, while the gas core presence at $Re \geq 1660$ results in a hollow cone liquid sheet. For the intermediate value $Re = 830$, the numerical simulations indicate a liquid sheet of mixed type. Consequences of the inflow asymmetry and Reynolds number to the uniformity

---

[*] Corresponding author
Email address: `erkki.laurila@aalto.fi` (E. Laurila)

Preprint submitted to International Journal of Multiphase Flow *August 31, 2018*

of the injected liquid mass distribution and liquid sheet instability are pointed out.

Keywords: pressure-swirl atomizer, primary atomization, hollow cone spray, two-phase flow, large-eddy simulation, volume-of-fluid method, LES, VOF, isoAdvector

---

1. Introduction

Atomization of liquids is of great interest in many practical applications such as fuel injection, spray painting, sprinkling, and fire suppression, to name a few. One widely used atomizer type is the pressure-swirl atomizer in which the fluid is forced into rotational motion before dispensing it from the nozzle. Consequently, flow rotation and centrifugal forces lead to the formation of an annular liquid sheet with gaseous core at the nozzle exit. Subsequently, a hollow cone spray is formed by the radially outward expanding liquid after it is discharged from the nozzle. Pressure-swirl atomizers are popular because of their geometrical simplicity, good atomization characteristics and resistance to clogging (Amini, 2016).

In the present study the main focus is on asymmetric inflow in contrast to so-called simplex nozzles where liquid is introduced to the nozzle commonly by symmetric inflow. However, with high relevance and close connection to the present study, we next describe certain aspects of such simplex nozzles as depicted in Fig. 1a. A typical simplex nozzle includes a cylindrical swirl chamber where two or more tangential inlet ports are connected. The cylindrical part of the swirl chamber is connected to an outlet orifice of a smaller radius with a conical section. The outlet orifice can be located directly after the conical section or it can be a cylinder of some finite length. A vast number of studies have been carried out on pressure-swirl atomizers and most of this research focuses on the simplex atomizer. Although the geometry of the nozzle in this study differs from a typical simplex nozzle, the operating principles are common for both nozzle designs.

The liquid sheet and primary breakup characteristics from simplex nozzles have been noted to be strongly dependent on the flow injection pressure. In other words, the injection velocity and hence the Reynolds number are important parameters in describing the spray characteristics. The spray develops through different stages depicted in Fig. 1c as injection pressure is increased and before a fully developed hollow cone spray is formed. According to Lefebvre (1989), such stages can be classified as follows: 1) the dribble stage, where liquid dribbles from the orifice; 2) the distorted pencil stage, where the liquid forms a distorted low speed jet; 3) the onion stage, where a cone is formed but retracted into a closed bubble by surface tension forces; 4) the tulip stage, where the bubble opens into a tulip shaped hollow cone with a ragged edge where large droplets are generated; and 5) the fully developed hollow cone spray, where the liquid sheet disintegrates relatively quickly after exiting the nozzle forming small droplets. Fig. 1b shows an example of such a hollow cone spray from the presently studied nozzle.

In fact, simplex spray characteristics have been noted to be closely linked to the internal flow governed by several non-dimensional quantities. Both the Reynolds number (ratio of viscous to inertial forces) as well as the swirl number (ratio of angular to axial momentum) have been noted to be of key relevance in spray characterization (Maly et al., 2018). The complete characterization of the internal flow depends on the geometry of the nozzle as the swirl number is dependent on the capability of the geometry to convert the linear inlet flow into rotational motion. The surface tension forces, indicated by the Weber number, can be shown to be insignificant for the internal flow (Chinn, 2008; Binnie and Harris, 1950). However, the Weber number is a key factor in the droplet dynamics of the resulting spray. The importance of gravity, and therefore Froude number, can be often considered to be negligible for typical small-scale atomizers, but may have a minor effect on large-scale nozzles (Chinn, 2008).

The internal flow of swirl atomizers has been studied intensively both theoretically and experimentally. Typically, authors aim at giving estimates for the film thickness, opening angle and exit velocity at the orifice. These quantities

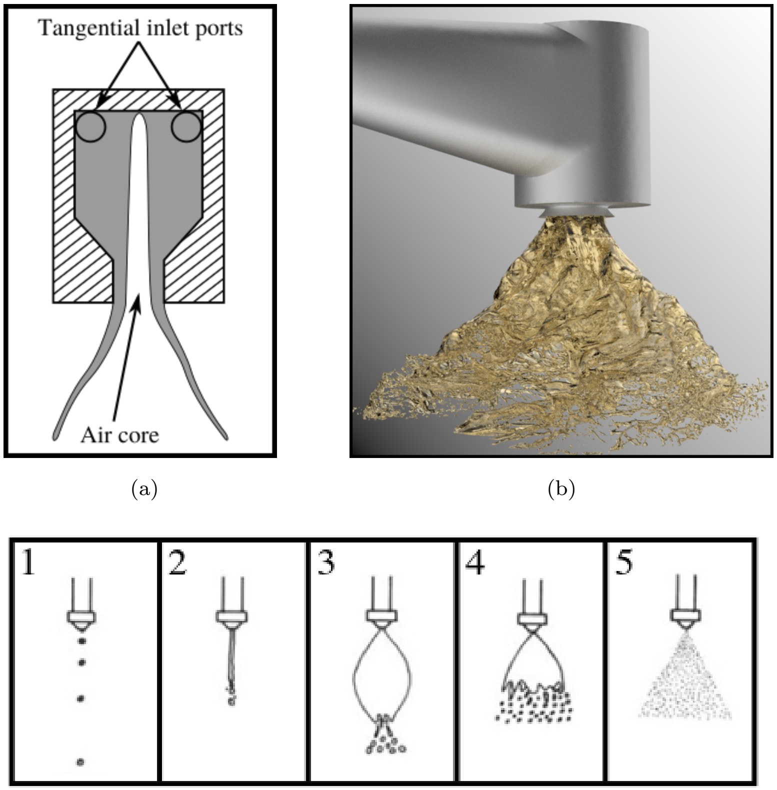

(a)

(b)

(c)

Figure 1: (a) A simplex atomizer with symmetric inlet positioning. (b) Hollow cone spray from a large-scale asymmetric swirl nozzle. A visualization from the present simulations. (c) The developing stages of the spray from a pressure-swirl atomizer as injection pressure is increased: 1) dribble stage, 2) distorted pencil stage, 3) onion stage, 4) tulip stage and 5) fully developed hollow cone spray. Schematic adapted from Lefebvre (1989).

can be subsequently used to predict the breakup of the liquid sheet. Semi-empirical correlations for the film thickness are given for example by Rizk and Lefebvre (1985) and Suyari and Lefebvre (1986). Some recent theoretical works include that by Amini (2016), where an analytical model is developed for the velocity fields inside a simplex atomizer, and the study of a tangential swirl atomizer by Wimmer and Brenn (2013), where the effect of viscosity on the flow rate is investigated.

Formation of an air core is a direct consequence of the nozzle hydrodynamics and is of vital importance in determining the film thickness and velocity at the nozzle orifice (Som, 2012). An overview of the air core characteristics is given in the review by Som (2012). The air core is formed when the pressure in the center of the vortex drops below the back pressure of the ambient air causing a suction effect for air entrainment into the vortex core. The formation of the air core exhibits two transitions as a function of the inlet flow Reynolds number. First, there is a critical Reynolds number, Re_{c1}, under which no air core is formed. When the Reynolds number is increased, the core develops because of the decreasing pressure in the vortex. The second critical Reynolds number, Re_{c2}, marks the condition when the core has reached a fully developed state. The inception of the air core depends on the radial pressure gradient caused by the swirl, and the swirl strength is, in turn, greatly influenced by the dimensions and geometry of the nozzle (Som, 2012).

For a typical simplex nozzle, the air core is cylindrical, whereas for an open-ended swirl nozzle the air core may exhibit a helical structure (Som, 2012). Experimentally, such helical structure has been observed by several authors, including Kim et al. (2009), Donjat et al. (2002) and Cooper and Yule (2001), while the phenomenon has also been demonstrated in CFD simulations by Dash et al. (2001). The variation of the air core may induce large fluctuations of the film thickness and affect the subsequent atomization process (Amini, 2016). However, the atomization models based on simple theoretical models usually consider the film stationary. Binnie and Harris (1950) studied the effect of surface tension for the dynamics of the air core theoretically and concluded that it is negligible. Numerical studies on pressure-swirl atomizer inner nozzle flow are numerous but relevant for this study are the works of Dash et al. (2001), Fu (2016), Galbiati et al. (2016b) and Renze et al. (2011).

The liquid film undergoes breakup after it is discharged from the nozzle. The breakup process can be divided into two parts: the primary atomization, where the continuous liquid sheet disintegrates because of instabilities, leading to the first generation of droplets; and the secondary breakup, where droplets repeatedly break into smaller droplets due to aerodynamic forces until a stable droplet size is reached (Ashgriz, 2011). Primary atomization is a highly complex process. Three mechanisms contribute to the breakup of the conical film from a swirl atomizer: sheet perforations, periodic fluctuations of the air core, and aerodynamic instabilities (Ashgriz, 2011). Most of the theoretical analysis of the breakup and breakup models are based on aerodynamic instabilities. The aerodynamic instability refers to a mechanism where small disturbances of the liquid sheet grow and finally cause the breakup of the sheet. The instability of a rotating annular liquid sheet has been first analyzed theoretically by Ponstein (1959), who derived a dispersion relation for the growth of disturbances in inviscid fluids. The results for growth of disturbances in planar sheets can be utilized when considering annular thinning sheets, as was done for example by Senecal et al. (1999) in their breakup model. The instabilities of the liquid film first break it into ligaments which further break into droplets (Ashgriz, 2011). The droplet size of the first generation of droplets is in the same order as the thickness of the liquid film (Ashgriz, 2011).

Theoretical work has been conducted on the instability and growth of disturbances. However, accurate information of the primary atomization is difficult to obtain by theoretical and experimental methods because of the high complexity of the process and the wide range of spatial and temporal scales involved. Computational tools offer a way to study the process from perspectives that are often inaccessible with experimental or analytical methods. Most computational primary atomization studies have considered round jets (Shinjo and Umemura, 2011; Yang and Turan, 2017), planar liquid sheets (Desjardins and Pitsch, 2010), or jets in cross flow (Herrmann, 2010; Li et al., 2017), while detailed computational studies on annular swirling liquid sheets have been more rare. Such studies include, for example, the paper by Ding et al. (2016) on the atomization mechanism of a hollow cone swirling spray in a typical simplex atomizer. They used the LES-VOF methodology and computed the spray at three different injection pressures and included the nozzle geometry in the simulation.

Fuster et al. (2009) applied a VOF method with adaptive mesh refinement

(AMR) to a hollow cone spray with analytical inlet conditions. They conducted a mesh refinement study and concluded that the mesh size can also influence the large-scale liquid structures of the flow. Galbiati et al. (2016a,c) conducted DNS studies of primary breakup of a conical swirled jet. They employed the VOF method with piecewise linear interface reconstruction for the advection of the phase interface. The nozzle geometry was not included in the simulation, but some of the simulations employed boundary conditions extracted from previous LES computations of a simplex nozzle. Shao et al. (2017) studied primary atomization of swirling liquid jet from an annular pipe and evaluated the effect of turbulent inlet conditions. They resolved the largest scales of the atomization and employed a mass conservative level set (MCLS) method for the advection of the phase interface. Also, the recirculation zone was investigated while a precessing vortex core was not observed in contrast to single phase swirling jets. Numerical studies considering primary atomization of conical swirled jets and the inner nozzle flow in pressure-swirl atomizers are summarized in Table 1.

In this paper a pressure swirl-atomizer is studied with large-eddy simulations and the volume-of-fluid method. A geometric reconstruction VOF scheme, `isoAdvector`, is used for interface capturing. Otherwise, the solution method is based on the `interFoam` solver of the OpenFOAM fluid dynamics library (Deshpande et al., 2012). The `interFoam` solver has been previously used for studying a pressure-swirl atomizer by Renze et al. (2011), while the `isoAdvector` scheme has been used for studying atomization in the context of fire suppression by Meredith et al. (2017). For more application examples of `interFoam`, see the references in the review by Deshpande et al. (2012).

The nozzle in the present study is used in industrial boilers to atomize fuels with high viscosity. The geometry of the nozzle (see Fig. 2) differs considerably from the standard simplex design which has been in the focus of many studies. The first noticeable difference is the scale of the nozzle. The discharge orifice diameter is in the centimeter range whereas simplex nozzles in typical applications are in the millimeter range or below (e.g. in Saha et al. (2012) and Yao et al. (2012)). More importantly, the current nozzle exhibits less symmetry than a typical simplex nozzle, where the small inlet ports (compared to the swirl chamber size) are located far upstream from the exit orifice. Such features enable flow development into rotational motion as noted by Galbiati et al. (2016b). In the current nozzle the inlet port is large (see Fig. 1b) which is expected to influence the symmetry of the flow field inside the swirl chamber. The asymmetry of the flow field may also affect the liquid film at the nozzle orifice which in turn greatly influences the onset of the atomization process.

LES has been chosen as a tool to study the nozzle because of the inherent time dependence of the primary atomization process. LES makes it also possible to capture the unsteady fluctuations of the liquid film at the discharge orifice caused by turbulence and other mechanisms. The relatively low Reynolds

Table 1: Positioning the present study in the context of previous numerical studies on primary atomization of conical swirled liquid jets (PA) and internal flow in pressure-swirl nozzles (IN). VOF-Geo refers to geometric interface reconstruction methods and VOF-Comp to methods employing compressive algebraic schemes for the interface.

Author	Theme	Int. capt.	BC for PA	Nozzle	Main focus
Galbiati et al. (2016a)	PA	VOF-Geo	Mean from LES/ Analytic	Simplex	Mesh refinement
Galbiati et al. (2016c)	PA	VOF-Geo	Mean from LES	Simplex	Jet instability/ Ligament analysis
Ding et al. (2016)	PA	VOF-Comp	Full nozzle incl.	Simplex	Injection pressure sweep
Shao et al. (2017)	PA	MCLS	Analytic/Turb. recorded	Annular pipe	Turbulent inlet/ Recirculation zone
Fuster et al. (2009)	PA	VOF-Geo AMR	Analytic	-	AMR mesh refinement/ Validation of methods
Dash et al. (2001)	IN	VOF-Comp	-	Simplex and open-ended	Air core
Fu (2016)	IN	VOF-Geo	-	Open-ended	Oscillating ambient pressure
Galbiati et al. (2016b)	IN	VOF-Comp	-	Simplex	Comparison to correlations/ Testing of turbulence models
Renze et al. (2011)	IN	VOF-Comp	-	Simplex and asymmetric	General features/ Non-Newtonian fluid
Present	IN/ PA	VOF-Geo AMR	Full nozzle incl.	Large-scale asymmetric	High viscosity fluid/ Instabilities at $Re \leq 5300$

numbers of the flow cases (420–5300, referred to the inlet pipe diameter) advocate a scale-resolving turbulence modelling approach. The inlet conditions and the role of turbulence have been recognized to be important for the onset of the breakup process in previous primary atomization studies (Salvador et al., 2018). One of the key benefits of solving both parts of the flow, i.e. the internal nozzle flow and the early parts of the primary breakup, is to have a realistic boundary condition at the nozzle discharge orifice.

To the authors' knowledge there are no previous computational studies of the present, or similar, large-scale tangential swirl nozzle. Especially the asymmetry of the geometry makes the current nozzle interesting in the light of its influence on the stability of the film and the resulting spray patterns. In addition, combined simulations of the full inner nozzle flow with also part of the primary atomization resolved are rare for swirling liquid atomization.

In this work the inner nozzle flow and the near nozzle spray are investigated in incompressible and iso-thermal conditions under the Newtonian fluid assumption. Four cases are simulated with laminar and turbulent inlet conditions and the structure of the flow field inside the nozzle is investigated. In addition, the large-scale instability and the onset of breakup of the liquid film are investigated in the near vicinity of the nozzle geometry. The main objectives of the paper are to:

1. apply the `isoAdvector` method in scale-resolving simulations of swirling liquid sheet atomization,
2. study a large-scale nozzle with significant asymmetric features,
3. carry out simulations with full coupling between the flow field inside the nozzle and the liquid sheet in the nozzle near field,
4. conduct a Reynolds number sweep and demonstrate the existence of spray pattern modes enriching the classical picture of the transitional spray patterns,
5. study the unsteady aspects of the atomization process including the variation of the air core and the large-scale unsteady modes of the liquid sheet,

6. quantify, (a) the unsteady effects inside the swirl chamber, (b) the film thickness at the orifice, (c) the variation of the film thickness, and (d) the uniformity of the mass flow distribution in the nozzle near field.

2. Numerical approach

2.1. Nozzle geometry

The nozzle geometry is shown in Fig. 2. The nozzle consists of a straight inlet pipe (I), an enlargement region (II), a cylindrical swirl chamber (III) and a discharge orifice (IV). A numerical recycling plane (V) has been defined in the inlet pipe to ensure realistic inflow conditions. The inlet pipe is 25 cm long, has a diameter of $D_p = 27$ mm and is inclined 45 degrees relative to the axis of the swirl chamber. The enlargement region redirects the flow from the inlet pipe to be tangential to the swirl chamber. The cross-section of the enlargement region changes from the circular inlet pipe to a flatter profile at the inlet port to the swirl chamber as indicated by Fig. 2. The height of the inlet port is slightly lower than the swirl chamber itself. The large size of the inlet port in respect to the swirl chamber poses an asymmetry to the internal nozzle flow and mass flow at the nozzle orifice.

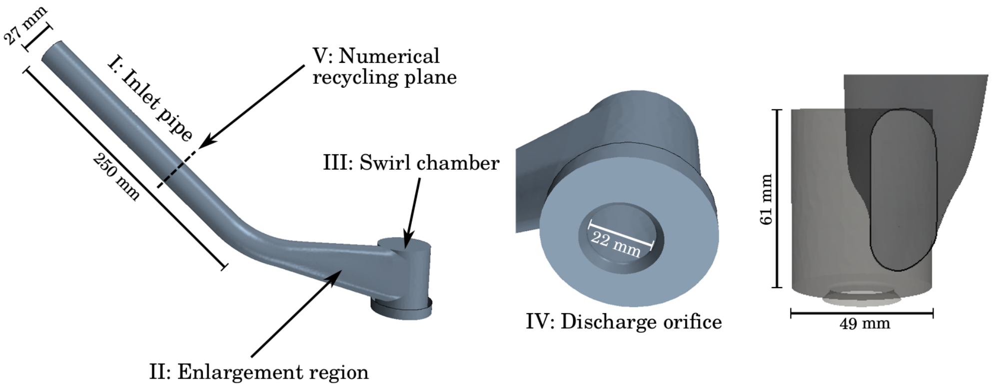

Figure 2: The nozzle geometry.

The incoming liquid is forced into a swirling motion by the swirl chamber wall. The height of the swirl chamber, H_s, is 61 mm and its diameter, D_s, is 49 mm. The swirling fluid finally exits the nozzle through the discharge orifice (IV) with a diameter $D_o = 22$ mm located at the bottom of the swirl chamber. The orifice is off-centered by 2 mm from the swirl chamber central axis towards the inlet port which also introduces an asymmetric component to the geometry.

2.2. Governing equations and numerical methods

The two-phase flow inside the nozzle and the near nozzle region is modelled with the VOF interface capturing approach by Hirt and Nichols (1981). Both the gas and liquid phases are considered as incompressible and immiscible, and the incompressible Navier-Stokes equations are solved for the conservation of mass and momentum:

$$\frac{\partial \rho}{\partial t} + \nabla \cdot \rho \boldsymbol{u} = 0 \tag{1}$$

$$\frac{\partial \rho \boldsymbol{u}}{\partial t} + \nabla \cdot \rho \boldsymbol{u}\boldsymbol{u} = -\nabla p + \rho \boldsymbol{g} + \nabla \cdot \left[\mu \left(\nabla \boldsymbol{u} + \nabla \boldsymbol{u}^T\right)\right] + \sigma \kappa \nabla \alpha \tag{2}$$

where $\boldsymbol{u}$, ρ, p, μ, σ, κ and α are the velocity, density, pressure, viscosity, surface tension, surface curvature and the indicator fields, respectively. The terms on the right hand side include the pressure gradient term, the gravitational body forces, and the viscous stresses, while the last term accounts for the capillary forces due to surface tension. In the VOF approach the movement of the gas-liquid interface is tracked by solving a scalar advection problem for the indicator field, α, which obtains a value of one in the liquid and zero in the gas phase. The equation for α is derived from Eq. 1 and yields:

$$\frac{\partial \alpha}{\partial t} + \nabla \cdot \alpha \boldsymbol{u} = 0 \tag{3}$$

The surface tension force is modelled using the Continuum Surface Force (CSF) approach of Brackbill et al. (1992) and the curvature of the interface is calculated from the indicator field as:

$$\kappa = -\nabla \cdot \left(\frac{\nabla \alpha}{|\nabla \alpha|}\right) \tag{4}$$

The density and viscosity of the two-phase mixture for the momentum equation are obtained as weighted averages of the corresponding gas and liquid properties:

$$\rho = \alpha\rho_l + (1-\alpha)\rho_g \tag{5}$$

$$\mu = \alpha\mu_l + (1-\alpha)\mu_g \tag{6}$$

where both the liquid and gas densities and viscosities are constant. The solver employs a modified pressure:

$$p_{rgh} = p - \rho\boldsymbol{g}\cdot\boldsymbol{x} \tag{7}$$

in the final formulation of the momentum equation (Deshpande et al., 2012). With this modification the pressure gradient and gravity terms in Eq. 2 are replaced by:

$$-\nabla p + \rho\boldsymbol{g} = -\nabla p_{rgh} - \boldsymbol{g}\cdot\boldsymbol{x}\nabla\rho \tag{8}$$

The governing equations are solved with the open source fluid dynamics library OpenFOAM (Jasak, 2009). The solution procedure follows the one employed in the `interFoam` solver (Deshpande et al., 2012), except for the method used for advecting the indicator field. First, the advection equation for α is solved, after which the material properties are updated and used in the momentum equation. The pressure-velocity coupling of the momentum equation is handled with the PISO (Pressure-Implicit with Splitting of Operators) algorithm.

LES has been applied for turbulence modelling. At low *Re* the solution inside the nozzle can be considered laminar and fully resolved, while at the two higher *Re* cases the relatively low Reynolds numbers advocate a scale-resolving strategy. As such a scale-resolving strategy, we employ the implicit LES (ILES) approach (Boris et al., 1992; Margolin et al., 2006; Grinstein and Fureby, 2007) by discretizing the convection term in the momentum equation with the non-linear flux limiting scheme of Jasak et al. (1999) similar to our previous work (Keskinen et al., 2016). The ILES approach has been successfully applied in a wide range of flow scenarios including homogeneous turbulence (Margolin et al., 2006; Aspden et al., 2008), free shear flows (Fureby and Grinstein, 1999; Xia and Tucker, 2012), wall bounded flows (Fureby and Grinstein, 2002; Keskinen et al., 2016), and in multiphysics applications such as reacting sprays (Wehrfritz et al., 2016; Kahila et al., 2018).

Outside the nozzle, resolving the length scales of the essential liquid structures is important. In the nozzle near field, the largest scales of the primary atomization and the initial liquid film thickness can be considered to be very well resolved. While the first generation of disintegrating liquid ligaments can still be captured, the thinning of the liquid film, the fine scale primary atomization or the possible secondary breakup are not adequately resolved in the present approach.

A geometric VOF method, `isoAdvector`, by Roenby et al. (2016) is used to advect the indicator field. The `isoAdvector` algorithm consists of two steps. First, the location and orientation of the phase interface are reconstructed inside computational cells intersected by the interface. This is achieved by using isosurfaces to divide the cells in relative proportions given by the local cell value of α. Second, the indicator field is advected by solving Eq. 3 explicitly for α at the next timestep. The projected subcell interface location during the timestep is used together with the fluid velocity to calculate estimates for the fluxes appearing in the discretized form of the convection term of Eq. 3. For the details of the implementation the reader is referred to Roenby et al. (2016).

2.3. Adaptive mesh refinement

Adaptive mesh refinement was used in a subset of the simulations to adequately capture the motion of the liquid interface near the nozzle. A tree-based AMR was used implying that each hexahedral cell marked for refinement is split into 8 smaller hexahedra and the procedure is repeated recursively on subsequent levels of refinement. In the present study two levels of refinement were used. The cell sizes and details of the AMR grid are further discussed in Section 2.5.

Here, the applied remeshing strategy aims at keeping the entire interface uniformly refined at the finest refinement level at all times. A relatively long remeshing interval (20 timesteps) is used to decrease the computational cost and to minimize the mapping errors from interpolating the fields between two levels of refinement. In the present simulations, the refinement is based on the value of the indicator field and activated in the cells which contain the interface. In addition, the cells in a three-cell-wide region adjacent to the interface cells are included in the refinement. Such a buffer region is used to avoid the advection of the interface outside the AMR region in the interval between remeshing. With the buffer width of three cells the remeshing interval was tuned to 20 timesteps. It was estimated (with conservative values of $U = 20$ m/s and $\Delta t = 5 \times 10^{-7}$ s) that the interface would advect approximately one cell width (0.2 mm) in a remeshing interval indicating that the liquid stays inside the finest refinement level. In summary, we expect that the present AMR procedure will only affect velocities in the gas phase. Thus, the high-density liquid inertia driven breakup process can be argued to be relatively insensitive to the AMR.

2.4. Domain and boundary conditions

The simulation domain consists of the nozzle interior and a cylindrical external environment as shown in Fig. 3a. The environment boundaries have been placed far from the nozzle in order to minimize boundary effects. The cylinder extends 1.0 m in the axial direction starting from the nozzle orifice and has a diameter of 1.0 m.

The boundary consists of three regions: the pipe inlet, the nozzle walls and the outlet condition for the environment as depicted in Fig. 3a. At the inlet, a Dirichlet condition of $\alpha = 1$ is imposed for the indicator field, while a Neumann condition (zero gradient) is used for p_{rgh}. A recycling technique is applied for the velocity. At each timestep the Dirichlet condition for the velocity is mapped from the recycling plane (V in Fig. 2) located $6D_p$ downstream of the inlet and scaled such that the mean inlet velocity is forced to the bulk velocity U_b. At the nozzle walls, Neumann conditions are applied for both p_{rgh} and α, while a no-slip Dirichlet condition is used for the velocity. At the outlet, a mixed

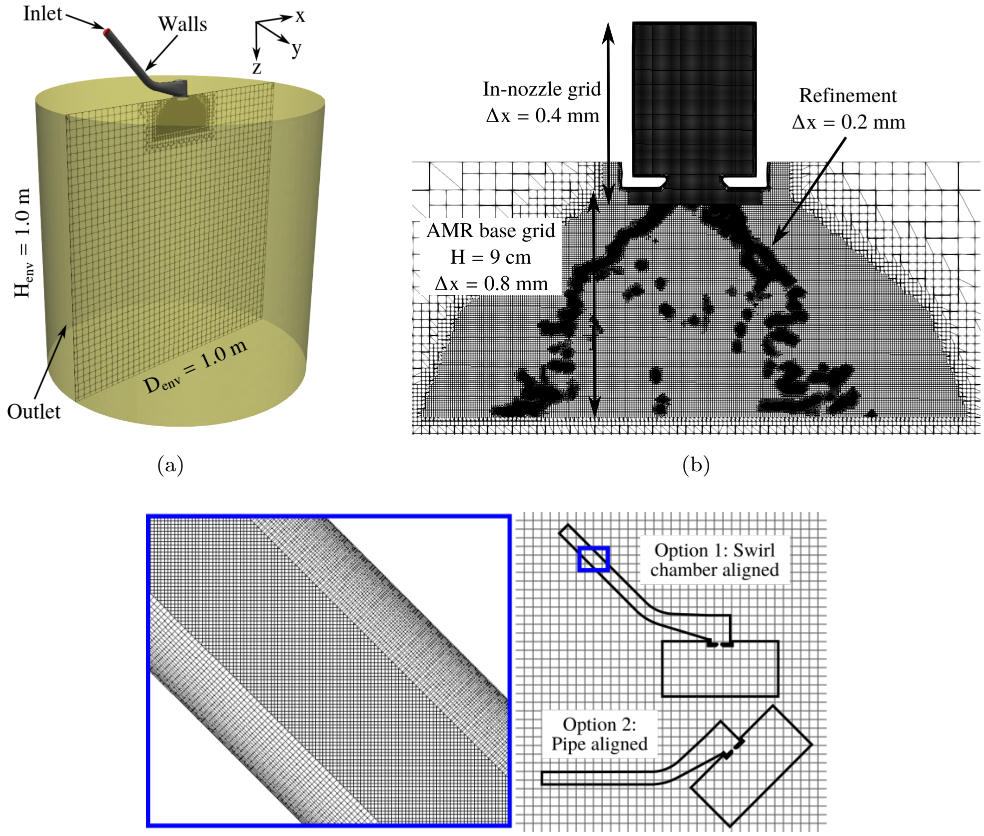

(a) (b)

(c)

Figure 3: (a) The simulation domain consists of the nozzle and a cylindrical outside environment. (b) The different static and adaptive refinement regions with respective cell sizes. (c) The hexahedral part of the mesh can be aligned either with the swirl chamber and the outside environment or with the inlet pipe (Option 1 is used in the present work). The close-up shows a cross-section of the grid at the inlet pipe.

type boundary condition is used depending on the direction of the flow. When the flow is into the domain, Dirichlet conditions are used for both the indicator field ($\alpha = 0$) and the velocity. In this case the velocity at the boundary is extrapolated from inside the domain. When the flow is out of the domain, Neumann conditions are used for α and $\boldsymbol{u}$. For both cases the total pressure of p_{rgh} is set to 0 Pa at the outlet boundary which fixes the pressure level inside the domain.

2.5. Computational grid

Here, we employed an unstructured grid consisting of a cartesian background grid together with a body-fitted boundary layer mesh. Such gridding strategy offers two logical options regarding the orientation of the background grid discussed in Fig. 3c. In Option 1 (2), the pipe flow direction is non-orthogonal (orthogonal) to the cartesian grid while the swirl chamber is orthogonal (non-orthogonal) to the grid. Here, Option 1 was chosen and the hexahedral part of the mesh was aligned with the coordinate system of Fig. 3a in order to provide best accuracy in the swirl chamber, exit orifice and nozzle near field regions. This choice, however, leads to a suboptimal grid in the inlet pipe region where the hexahedral cells in the central part of the pipe are non-orthogonal to the main flow direction (see the close-up in Fig. 3c). The mesh non-orthogonality has an effect on the velocity statistics at the inlet pipe as will be further quantified in Section 3.1.1.

The wall refinements in the pipe flow region are such that the width of the first cell is $y^+ \approx 1$ and there are approximately 7 cells in the region $y^+ < 10$, when y^+ refers to the wall coordinate defined with the friction velocity at $Re = 5300$ conditions. While the wall layer can be considered to be well resolved for $Re \leq 1660$, the conditions above do not fully comply to the highest Reynolds number case near the exit orifice.

The mesh resolution was chosen based on the accuracy requirements needed to capture the essential turbulent and droplet length scales. Before conducting the final simulations presented in this paper, precursor simulations were run on coarser grids as will be later discussed. From these simulations the stable droplet size was estimated to be approximately 1.9 mm. Based on this estimate the cell size in the near nozzle region was chosen to be $\Delta x = 0.2$ mm implying that the stable droplet is resolved with approximately 10 cells. This, in turn, leads to a cell size of $\Delta x = 0.4$ mm for the hexahedral cells inside the nozzle. The advantages and disadvantages of the present method/resolution in capturing the smallest droplets are further elaborated in the final part of the results.

Two grids were created for the simulations. Both have an identical mesh inside the nozzle but contain differences in the mesh of the near field. The first grid has approximately 8.2 million cells and does not include a refinement in the near field region. This grid was used for longer averaging runs to obtain statistics on the inner nozzle flow. The second grid has a uniform refinement in the near field region and was used in the coupled simulations incorporating the accurate interface capturing in the near field by AMR. This so-called AMR base grid contains 11.4 million cells and is shown in Fig. 3b.

Two levels of AMR were used which indicates an unrefined cell size of $\Delta x = 0.8$ mm in the nozzle near field. The AMR was enabled only in the near field in a region extending 9 cm from the orifice at $Re = 420$ and 7 cm in the other cases. The exact plane marking the beginning of the AMR region is located 7 mm below the nozzle orifice exit plane. The spatial extent of the AMR base grid was chosen based on the available computational resources while ensuring that the region relevant for the onset of primary atomization was covered. The sparse background grid outside the AMR refinement region is not fine enough to resolve the individual droplets moving from the refined to the sparse region. However, the sparse grid captures the downstream average mass flow distribution approximatively, and therefore effectively acts as a realistic boundary condition for the refined near field region. With the AMR enabled the cell count of the different simulations varied roughly between 20-26 million cells.

2.6. Simulation cases

Four cases have been simulated with different Reynolds numbers by changing the viscosity of the fluid. Here, the Reynolds number refers to the bulk Reynolds number of the inlet pipe defined by the mean inlet velocity, $Re = \rho_l U_b D_p / \mu_l$. The cases are chosen such that the first three cases are in the laminar regime, considering the inlet pipe flow, and such that the Re approximately doubles between the cases. The inlet pipe flow for the highest Re case is in the fully

Table 2: Overview of the different simulation cases.

Re	μ_l [mPas]	Inlet pipe flow	Swirl chamber turbulence level	Air core	Near field spray pattern
420	395	Laminar	Laminar	No	S-sheet
830	200	Laminar	Laminar, unsteady	No	In transition
1660	100	Laminar	Moderately turbulent	Yes	Hollow cone
5300	31.2	Turbulent	Fully turbulent	Yes	Hollow cone

turbulent regime as the transition in pipe flow occurs approximately at $2000 < Re < 4000$ (White, 2006).

The simulated cases are summarized in Table 2 with characteristic details. All parameters, excluding the liquid viscosity, are held constant in the simulations. This indicates that also the liquid Weber number referred to the nozzle orifice, $We = D_o U_b^2 \rho_l / \sigma = 8400$, is constant between the cases. In all cases the surface tension was $\sigma = 0.07$ N/m, liquid and gas densities $\rho_l = 1406$ kg/m^3 and $\rho_g = 1$ kg/m^3, gas viscosity $\mu_g = 0.0148$ mPas, and the mean inlet velocity $U_b = 4.36$ m/s.

Two simulations have been run for each case: a longer run without the AMR refinement in the near nozzle region to gather statistics inside the nozzle; and a shorter run with the near nozzle refinement and AMR enabled. The non-dimensional simulation times of the longer averaging runs were $T = 0.95$, 0.98, 1.06 and 2.42 for the different cases at $Re = 420$, 830, 1660 and 5300, respectively. Above, the times have been non-dimensionalized with a reference flow through time, $T_{FT} = 0.1$ s which represents the approximate time it takes for the flow to advance from the pipe inlet to the nozzle orifice with the mean velocity U_b. Timestep adaptation was used in order to keep the maximum Courant number at the value 0.5 in the simulations without AMR and at 0.15-0.3 in the simulations with AMR.

The initial conditions for the simulations have been obtained from the precursor simulations. The simulations were initialized with a coarse grid and this solution was then mapped to a denser grid. The cases have been simulated on a series of coarse (650k cells), intermediate (3.6M cells) and dense meshes (8.2M cells) to allow the initial flow field to develop into a statistical steady state before conducting the final simulations on the dense mesh.

3. Results and discussion

3.1. Flow inside the nozzle

3.1.1. Flow in the inlet pipe

The mean velocity and turbulence profiles in the inlet pipe are shown in Fig. 4. When $420 \leq Re \leq 1660$ the flow is in the laminar regime matching with the analytical Poisseulle solution. At $Re = 5300$ the inflow is fully turbulent and close to the DNS data by El Khoury et al. (2013) at the same Reynolds number ($Re_\tau = 180$). The velocity fluctuation statistics, on the other hand, deviate more from the DNS. Near the center line of the pipe the levels of the fluctuations are generally well predicted, but in the wall vicinity the profiles differ more. In Fig. 4b the profiles are non-dimensionalized with the friction velocity, $u_\tau = \sqrt{\tau_w/\rho}$, which has been calculated from the simulation data for each case. Perfect correspondence of the statistics is not expected as the grid is non-orthogonal to the pipe axis and, therefore, to the principal flow direction at the inlet pipe (see Option 1 in Fig. 3c) which effectively leads to a loss of numerical resolution. In addition, the vicinity of the enlargement region to the recycling plane may permit a subtle upstream-downstream coupling via pressure.

At $Re \leq 1660$, the inlet velocity profiles closely match with the analytical reference solution. For completeness, we next discuss the small deviation between the DNS data and the present LES at $Re = 5300$. First, it may be possible that the swirl chamber affects the pipe flow statistics. A numerical test on the same inlet pipe grid of length $9D_p$ without the chamber was observed to provide approximately the same statistics (not shown here). In the test, the recycling technique was utilized again and the flow was allowed to exit from the

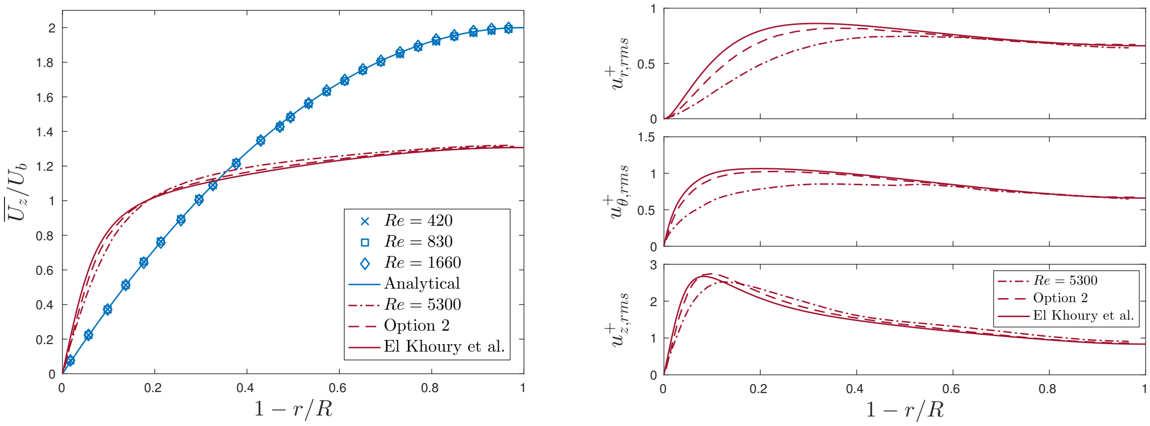

(a) (b)

Figure 4: (a) The mean velocity profiles for all the cases and (b) the fluctuation statistics for the $Re = 5300$ case at a cross-section plane of the inlet pipe $6D_p$ from the pipe inlet. The turbulent profiles are compared to the pipe flow DNS data of El Khoury et al. (2013) and laminar profiles to the analytical Poisseulle solution. Also, an additional simulation of turbulent pipe flow at $Re = 5300$ (Option 2) is provided to illustrate the effect of the grid non-orthogonality on the statistics (see Fig. 3c).

downstream end of the pipe. The conclusion is that the swirl chamber seems to have only a subtle effect on the pipe flow statistics. Second, it may be possible that the grid orientation impacts the flow statistics (see the two options in Fig. 3c). To assess such orientation effects an additional simulation of the turbulent pipe flow at $Re = 5300$ with a mesh fully aligned with the pipe axis was carried out (Option 2 in Fig. 3c). The results are depicted in Fig. 4 and they indicate that the grid non-orthogonality has an impact on the statistics and the results improve substantially when the flow is orthogonal to the grid.

The results indicate that the used numerical method and grid resolution are sufficient, especially in regions where the grid is well aligned with the geometry. The meshing strategy utilized here (Option 1 in Fig. 3c) aims at optimizing the grid quality in the critical parts of the domain, namely in the swirl chamber, exit orifice and near nozzle regions, at the expense of resolution in the inlet pipe. The velocity statistics can be also examined in light of earlier studies employing ILES for wall bounded flows (Fureby and Grinstein, 2002; Keskinen et al., 2016). The present findings are consistent with the results of Keskinen et al. (2016) on turbulent pipe flow at $Re_\tau = 360$ using the same ILES strategy on comparable grid resolution.

Regardless of the non-ideal grid orientation and the possible downstream interference, the velocity statistics at the inlet pipe show relatively good correspondence to the DNS data. Thereby, we consider that the effective boundary condition for the swirl chamber to be reasonably good for even the highest Reynolds number. Importantly, the test above provides numerical evidence on the potential of the used ILES approach and numerical resolution in the present cases.

3.1.2. Flow in the enlargement region

The mean and instantaneous velocity magnitude across the inlet pipe and the enlargement region are visualized in Fig. 5. At $Re = 420$ the mean and instantaneous velocity fields are nearly identical with minor fluctuation. As the Reynolds number is increased the fluctuations start to become more prominent in particular inside the swirl chamber. At $Re = 1660$ the fluctuations are prevalent in the swirl chamber and start to manifest in the enlargement region as well, even though the inlet flow is fully laminar. Finally, at $Re = 5300$ the entire flow field is turbulent.

The prominent feature in all the cases is the low velocity region (I in Fig. 5) in the upper part of the enlargement region. The high velocity fluid stream from the inlet pipe (II in Fig. 5) continues along the bottom of the inlet channel after the pipe bend. The bend in the pipe also generates a pair of counter-rotating secondary flow structures, called Dean vortices (I in Fig. 7) (Ito, 1987). The vortices are generated when the high velocity fluid at the central part of the pipe is pushed towards the bottom part of the bend by centrifugal forces. Such an effect causes the low velocity fluid near the walls to move upwards to the low pressure region near the top part of the bend thus generating the vortices.

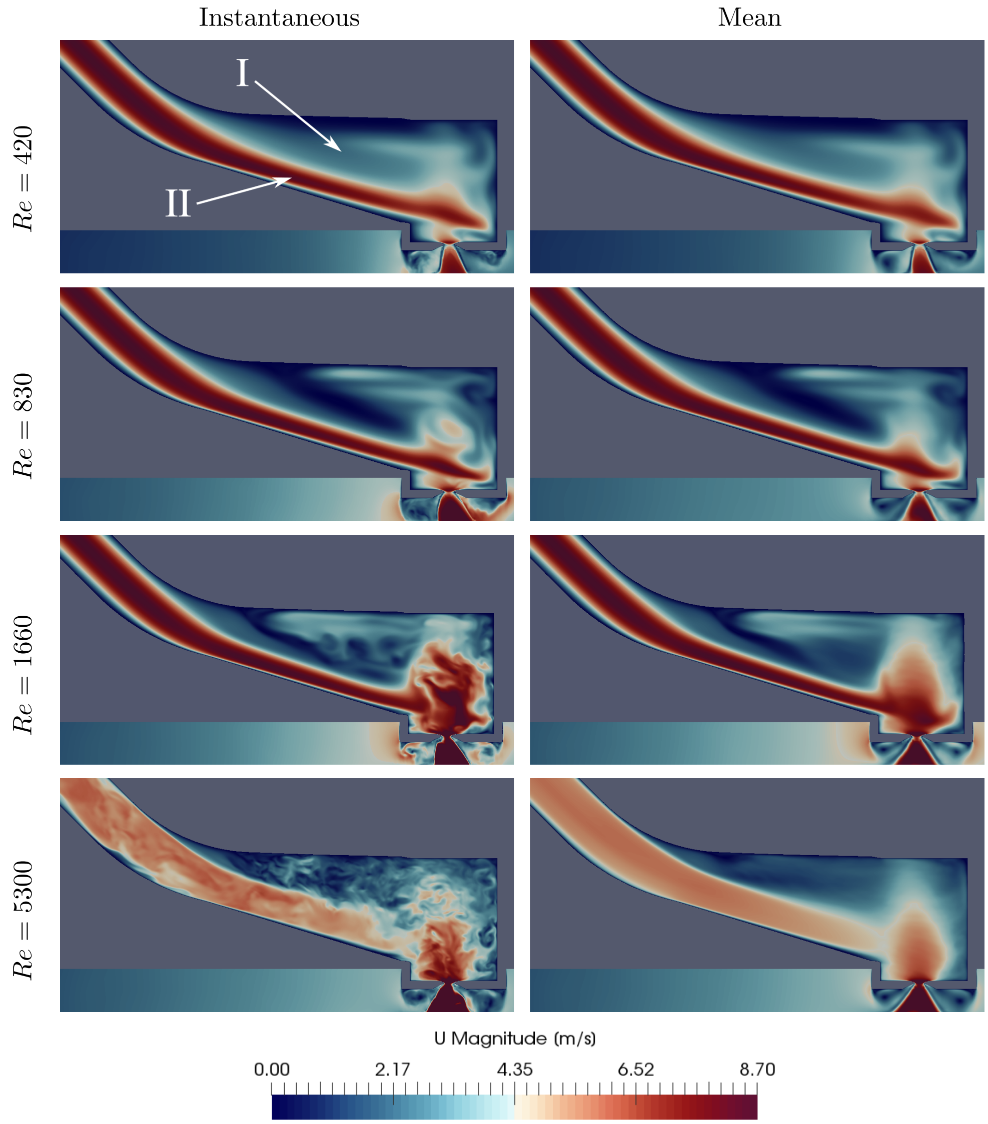

Figure 5: Instantaneous and mean velocity magnitude at the enlargement region and swirl chamber. The plane aligns with the axis of the inlet pipe and does not intersect with the air core inside the chamber.

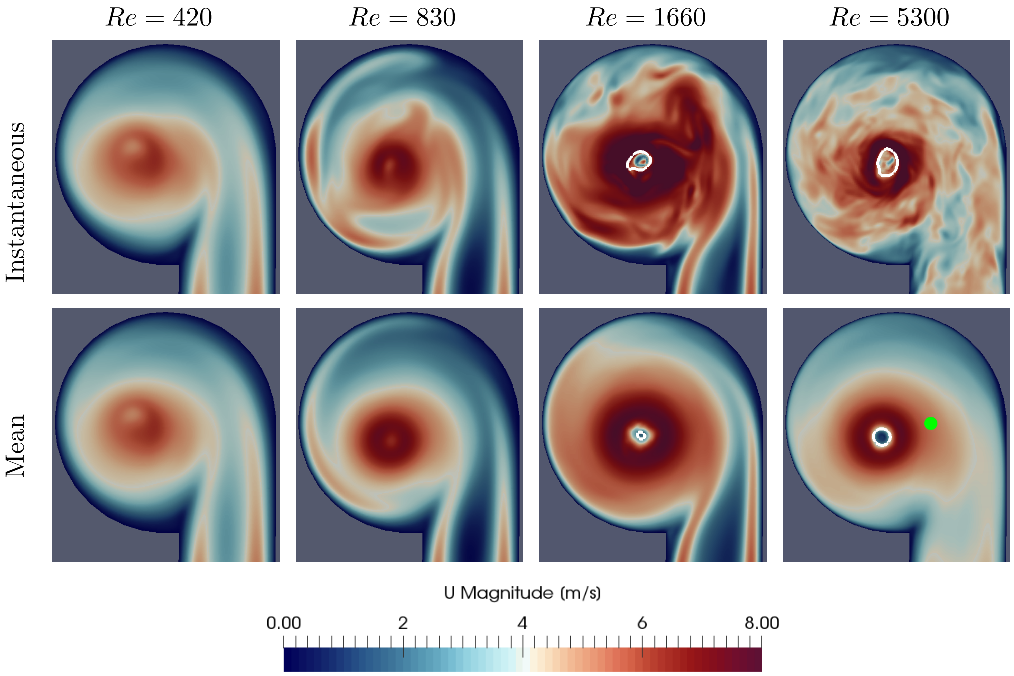

Figure 6: Instantaneous and mean velocity magnitude at the swirl chamber. The plane passes through the vertical midpoint of the chamber. The location of the phase interface is illustrated with the white line, while the green dot ($Re = 5300$ mean) indicates the location of the velocity probe of Fig. 8.

3.1.3. Swirl chamber: Flow characteristics

The mean and instantaneous velocity magnitudes at the midplane of the swirl chamber of Fig. 6 indicate flow character for the different Reynolds numbers. At $Re = 420$ the flow remains laminar and almost stationary, while at $Re = 830$ more fluctuations can be noted in the vortex inside the chamber. At $Re = 1660$, the laminar inflow is observed to transition to turbulent-like structures in the swirl chamber, while at $Re = 5300$ the flow is fully turbulent both in the inlet pipe and inside the chamber. Similar to simplex nozzles, the air core appears at $Re \geq 1660$. Here, the center of rotation of the vortex is shifted from the axis of the chamber as a result of two factors. First, the location of the outlet orifice does not coincide with the chamber axis because of the small offset towards

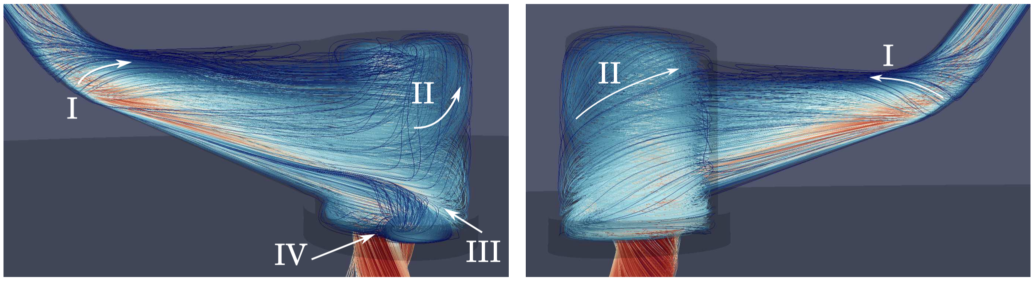

(a) (b)

Figure 7: Streamlines of the mean velocity field at $Re = 420$ colored by the velocity magnitude. The front (a) and back views (b) of the nozzle show the Dean vortices at the pipe bend (I), upward motion of the flow near the swirl chamber wall (II), the impingement point (III) where the inlet stream impinges on the wall, a second impingement point (IV) and the counter flow between the points III and IV.

the inlet port. Second, the inlet stream from the inlet port pushes the vortex towards the opposite side of the chamber.

Streamlines of the mean velocity field of the laminar $Re = 420$ case in Fig. 7 are used to visualize some features of the inner nozzle flow common to all the cases. Double Dean vortices are generated at the pipe bend (I) as was discussed earlier. This vortex structure is common to all the cases and also visible in the mean field of the turbulent $Re = 5300$ case. The high velocity inlet stream enters the swirl chamber relatively close to the bottom of the chamber. The stream generates a layer of liquid near the walls of the chamber, where the mean axial motion becomes upwards-oriented as is indicated by the streamlines (II). Such a layer is seen in all the cases. Close to the center of the chamber, the axial velocity component points generally downward towards the orifice and increases as the center of the vortex is approached.

An impingement point (III) is created at the wall opposite of the lower part of the inlet port as the liquid hits the wall. The impingement point is present in the cases with laminar inflow and it is caused by the higher peak velocities of the inlet stream. The impinging stream causes the fluid to flow opposite to the general direction of the swirl near the bottom of the chamber between the

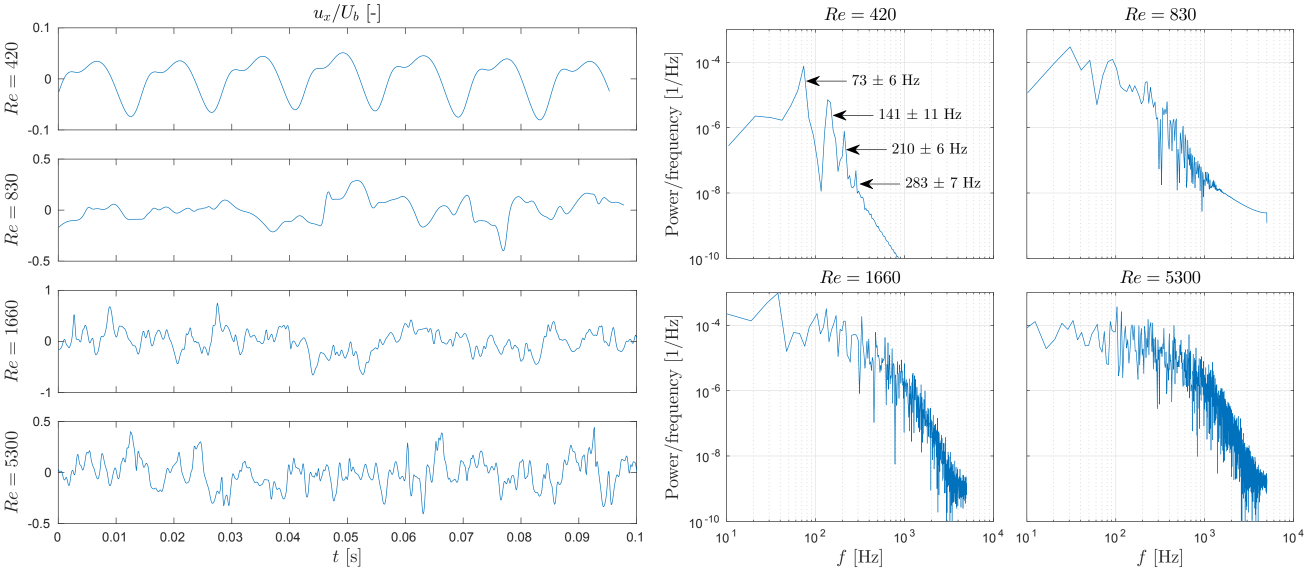

(a)

(b)

Figure 8: (a) The x-component of the velocity fluctuation taken at a single point at the midplane of the swirl chamber. The location of the point is indicated in Fig. 6. (b) The corresponding power spectra of the velocity signals. A slow periodic oscillation with a characteristic frequency of $f = 73 \pm 6$ Hz is exhibited at $Re = 420$.

points III and IV. This leads to the formation of a second impingement point at the point IV, because the motion of the liquid is in the general direction of the swirl in the rest of the lower chamber. These flow features near the bottom of the chamber affect considerably the velocity field close to the outlet orifice and have therefore an effect on the spray pattern as will be shown later on in the paper. The reverse flow region between the points III and IV is visible in the mean fields of all the cases except $Re = 5300$, although the locations of the impingement points vary between the cases.

Fig. 8 shows a time series of the x-component of the velocity fluctuation taken at a single point at the swirl chamber midplane (see Fig. 6) in the different cases. The power spectral densities of the corresponding velocity signals are also depicted in the figure. At $Re = 420$, the spectrum features distinct frequency peaks as also noted from the time series. When Re increases the spectra are seen to become continuous. Although the flow fluctuates significantly at $Re = 830$, high frequency components ($\gtrsim 1.5$ kHz) are not present as is evident from the spectrum. The spectra also indicate that the majority of the energy is contained in the low frequency components of the fluctuations.

At $Re = 420$ the fundamental frequency turns out to be $f = 73 \pm 6$ Hz while higher harmonics are noted as well. Above, the error estimate is taken to be the half width at the half maximum of the frequency peak. In non-dimensional form, the frequency can be expressed in terms of the flow Strouhal number:

$$St = \frac{f D_s}{U_b} \tag{9}$$

where D_s is the diameter of the swirl chamber and U_b is the mean inlet velocity. It is noted that $St = 0.82$. A value close to unity indicates that the fundamental frequency may originate from the flow dynamics inside the chamber.

3.1.4. Swirl chamber: Air core

The air core is a prominent feature of the flow in the swirl chamber at $Re = 1660$ and 5300. Generally, the air core is slightly off-centered from the axis of the chamber. The simulation results indicate, that the location and size of the core may fluctuate depending on the surrounding flow conditions.

Helical structure with two edges is visible on the liquid-gas interface of the air core as depicted in Fig. 9. In fact, the cross-section of the helix is somewhat flattened, i.e. elliptical in shape. Based on visual inspection, we note that the interface represents a wavelength structure of approximately $\lambda_h \approx 2H_s/3$. The waves travel in a spiraling manner towards the nozzle orifice. Similar helical structures of the air core have been previously observed by several authors. Based on their experimental work on large-scale simplex atomizers, Donjat et al. (2002) noted that the placement of the inlet ports and the nozzle geometry strongly affect the structure of the air core. Cooper and Yule (2001) also observed an effect of the number of the inlet ports on the resulting wave pattern. In the experiments two inlet ports led to a clear helical pattern with two edges, while a more obscure

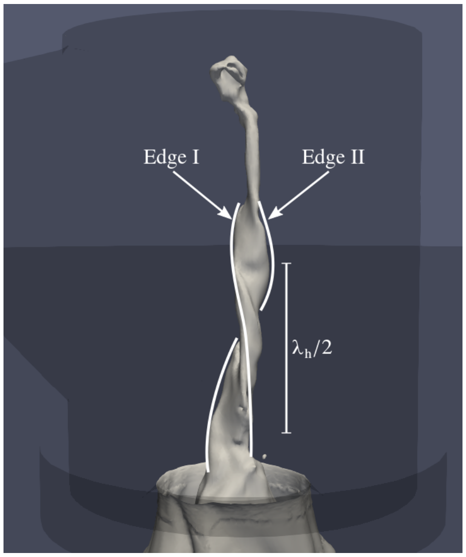

Figure 9: An instantaneous surface of the air core showing the helical structure at $Re = 5300$. The two edges of the helix (wavelength λ_h) have been highlighted in the picture.

pattern with multiple edges was noted in the case with eight inlet ports. The authors also observed liquid film breakdown in which the air core touched the wall of the orifice resulting in a disruption of the sheet. Such a breakdown was not observed in the current simulations. However, the previous research and the current simulations suggest that the fluctuations caused by the helical air core structure influence the liquid film fluctuation at the orifice.

3.2. Flow at the nozzle orifice

3.2.1. Overview

The mean film thickness and fluid velocity distribution at the discharge orifice are very important in the breakup process. In addition, the turbulent velocity fluctuations at the nozzle orifice cause initial perturbations to the liquid sheet which influence the subsequent primary atomization. For example, the turbulence characteristics have been noted to have a large impact on the atomization process in the context of round jets (Salvador et al., 2018). The annular fluctuating film becomes thinner as it progresses downstream of the

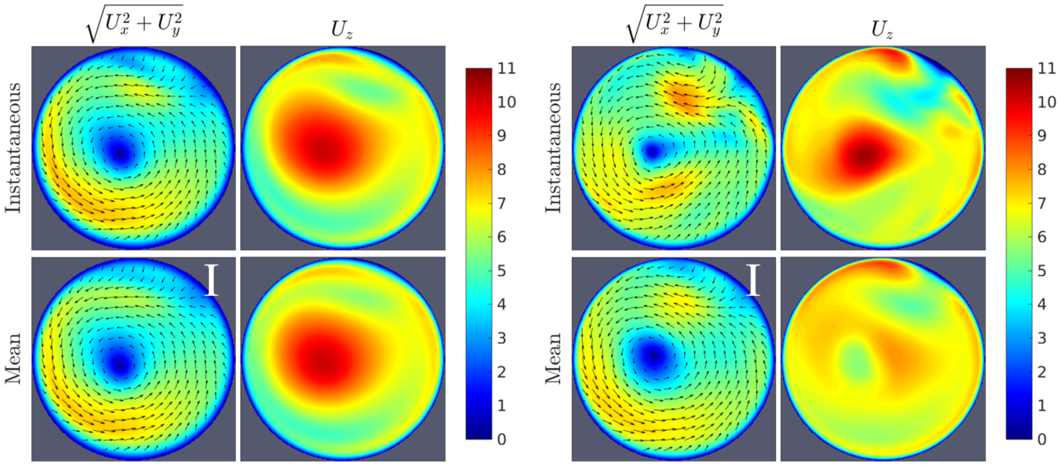

(a) $Re = 420$ (b) $Re = 830$

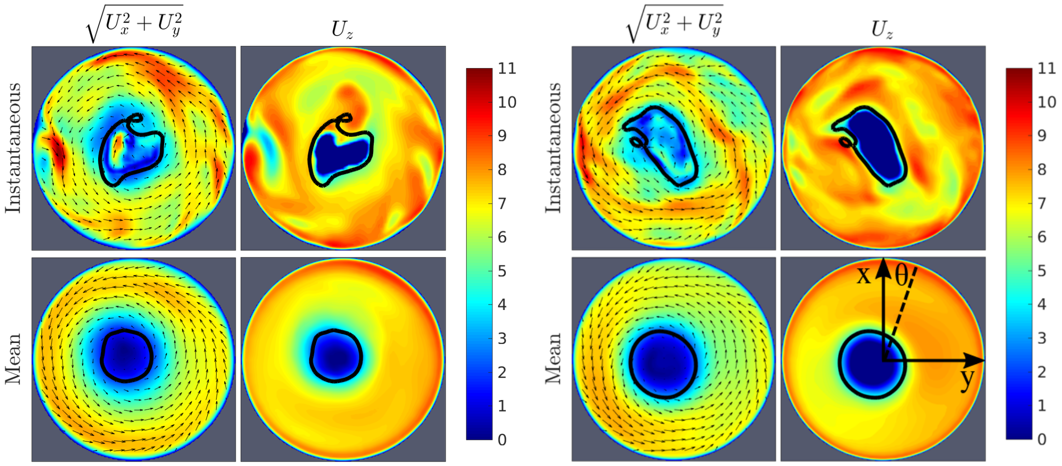

(c) $Re = 1660$ (d) $Re = 5300$

Figure 10: Axial and in-plane velocity fields at the nozzle orifice. The position of the liquid interface is indicated with a black line in the cases where the air core is present. The line of sight is from top of the chamber towards the orifice and the inlet flow direction in the x-direction. Note that the velocity scale is cut at 0 and thus the negative velocities in the air core are not shown.

nozzle. Clearly, the initial film thickness influences the location where the disintegration starts. Several factors, such as the nozzle geometrical parameters and the inlet Reynolds number, have been noted to impact the film thickness (Som, 2012). An increase in the inlet Re generally results in a decrease in the film thickness (Som, 2012).

Next, the flow conditions are studied at the nozzle orifice. Fig. 10 shows velocity distributions at the discharge orifice. The orifice plane is taken to be at the level where the area of the rounded nozzle orifice is the smallest. Both the mean and instantaneous fields are shown in the figure. The cut planes indicate the asymmetry of the flow field at the orifice. The center of the vortex is shifted towards the lower left corner in the figures creating an uneven flow distribution. The presence of the air core causes the axial velocity fields at $Re = 1660$ and 5300 to differ considerably from the ones observed at $Re = 420$ and 830. In the cases without the core, the axial velocity obtains its maximum value near the center of the orifice. At $Re = 1660$ and 5300, where the air core is present, the mean axial velocity at the core center is negative (order of 4 m/s at $Re = 5300$): air is drawn into the vortex from the center and returns near the liquid film.

As was described in Section 3.1.3, an impingement point is formed at the wall of the swirl chamber in the cases with laminar inlet stream (III in Fig. 7), and a counter rotating flow structure is formed near the bottom of the chamber (from III to IV in Fig. 7). The effect of this structure is clearly visible in the mean and instantaneous fields at the nozzle orifice near the point I in Figs. 10a and 10b. The in-plane velocity vectors are directed more towards the center of the orifice in this region as compared to the rest of the circumference where the velocity has a larger tangential component.

3.2.2. Liquid film thickness

Here, liquid film is observed to form at $Re \geq 1660$. The film position ($\alpha = 0.5$) is indicated in Fig. 10 with black lines. Two observations can be made from the average fields: the center of the air core is not located at the center of the outlet orifice but the core itself is circular. However, the instantaneous shape of the core is not circular. The shape and position of the core change considerably as a function of time. For example, an elliptical interface contour

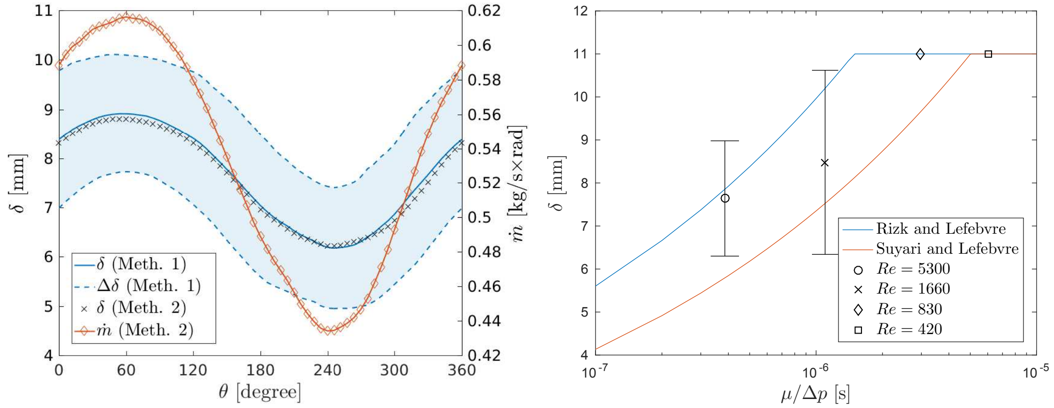

(a)

(b)

Figure 11: (a) The film thickness δ, its standard deviation $\Delta\delta$ (blue area), and the mass flow $\dot{m}$ as functions of the azimuthal angle θ at the nozzle orifice in the $Re = 5300$ case. Film thickness is insensitive to the data analysis method (Method 1: snapshot based, Method 2: time average based). (b) Mean film thicknesses and mean standard deviations (error bars) from the simulations compared to analytical correlations for simplex atomizers. Here, the mean indicates averaging also over the azimuthal angle θ.

can be observed rotating in the direction of the swirl at $Re = 5300$. Such a shape is qualitatively consistent with a somewhat flattened air core topology shown in Fig. 9.

Time variation of the air core at $Re = 5300$ is quantified in Fig. 11a. The figure shows the film thickness as a function of the azimuthal angle at the outlet orifice, with θ and the coordinate system defined according to Fig. 10d. The shift in the position of the air core center causes the time averaged film thickness to vary considerably as a function of the angle. The thickness reaches its maximum at approximately $\theta = 60°$ which corresponds to the location where the inlet stream impinges the back of the swirl chamber. The minimum film thickness is observed on the opposite side of the orifice ($\theta = 240°$). The mean thickness of the film averaged over the angle θ is presented in Table 3.

The variation of the film thickness as a function of time has been quantified by the standard deviation of the thickness in Fig. 11a. The standard deviation

Table 3: The film thickness, δ, the standard deviation of the thickness, $\Delta\delta$, and the discharge coefficient, C_d.

Re	δ [mm]	$\Delta\delta$ [mm]	C_d
420	-	-	0.68
830	-	-	0.67
1660	8.48	2.14	0.58
5300	7.64	1.34	0.61

has been calculated separately for each angle θ from the series of instantaneous snapshots of the α field at the orifice. Fig. 11a illustrates that the variation does not significantly depend on the azimuthal angle θ at $Re = 5300$. The mean deviation averaged over the angle θ is shown as the error bars in Fig.11b, where it is seen, that the thickness varies considerably with time: 18% at $Re = 5300$ and 25% at $Re = 1660$.

Fig. 11a also shows the mass flow as a function of θ calculated as:

$$\dot{m}(\theta) = \frac{1}{\Delta\theta} \int_0^{R_o} \int_\theta^{\theta+\Delta\theta} \rho U_z r d\theta dr \tag{10}$$

where the time averaged velocity and indicator fields have been used in the calculation. The mass flux follows the film thickness closely as the axial velocity distribution is reasonably uniform at $Re = 5300$.

Estimates for the film thickness at the orifice are needed in engineering and design considerations. Typically estimates are obtained from correlations based on theoretical models and experimental measurement data. A widely used correlation for simplex nozzles is of the form:

$$\delta = C \left(\frac{D_o \dot{m} \mu}{\rho \Delta p} \right)^{1/4} \tag{11}$$

where the constant C is 3.66 according to the original correlation of Rizk and Lefebvre (1985), or a corrected value of $C = 2.7$ according to Suyari and Lefebvre (1986) which has been found to better match experimental data. These correlations are plotted in Fig. 11b and comparisons are made to the film thicknesses from the simulations. The simulation results are fairly well in line with the estimates given by the correlations. The correlation of Rizk and Lefebvre (1985) predicts film thicknesses greater than the radius of the orifice for the two lowest Re cases where indeed no air core is observed. The correlation of Suyari and Lefebvre (1986) on the other hand would estimate the air core to be present also at $Re = 830$. It should be kept in mind that neither of the correlations have been intended for predicting the formation of the air core. It should be noted that the selection of points for the pressure difference is somewhat arbitrary both in the current simulations and in general application of the correlation. Here, the pressure difference has been calculated between the reference back pressure outside the nozzle and the mean pressure at the center line of the inlet pipe $6D_p$ from the inlet plane.

In addition to the film thickness analysis, we report the discharge coefficient (C_d) values in Table 3. The discharge coefficient has been calculated as the ratio of the actual volumetric flow rate Q and the flow rate predicted by the inviscid theory:

$$C_d = \frac{Q}{A_o\sqrt{\frac{2\Delta p}{\rho}}} \tag{12}$$

Here, A_o is the area of the orifice and Δp the pressure difference over the nozzle. Same definition for the Δp has been used here as in Eq. 11. The calculated discharge coefficient is in the range 0.58-0.68. In comparison to the correlation by Rizk and Lefebvre (1985) these values are higher. The correlation depends only on the nozzle geometrical parameters and gives a value of 0.31 for the current nozzle geometry.

3.3. Flow in the nozzle near field

3.3.1. Overview

The liquid film in the nozzle near field is visualized with the iso-surface $\alpha = 0.5$ in Fig. 12 from different viewing angles. The figure depicts representative snapshots of the film at individual time instances and includes only the interface in the refined part of the simulation domain in the visualization. The shape of the spray changes considerably as a function of the Reynolds number. The four

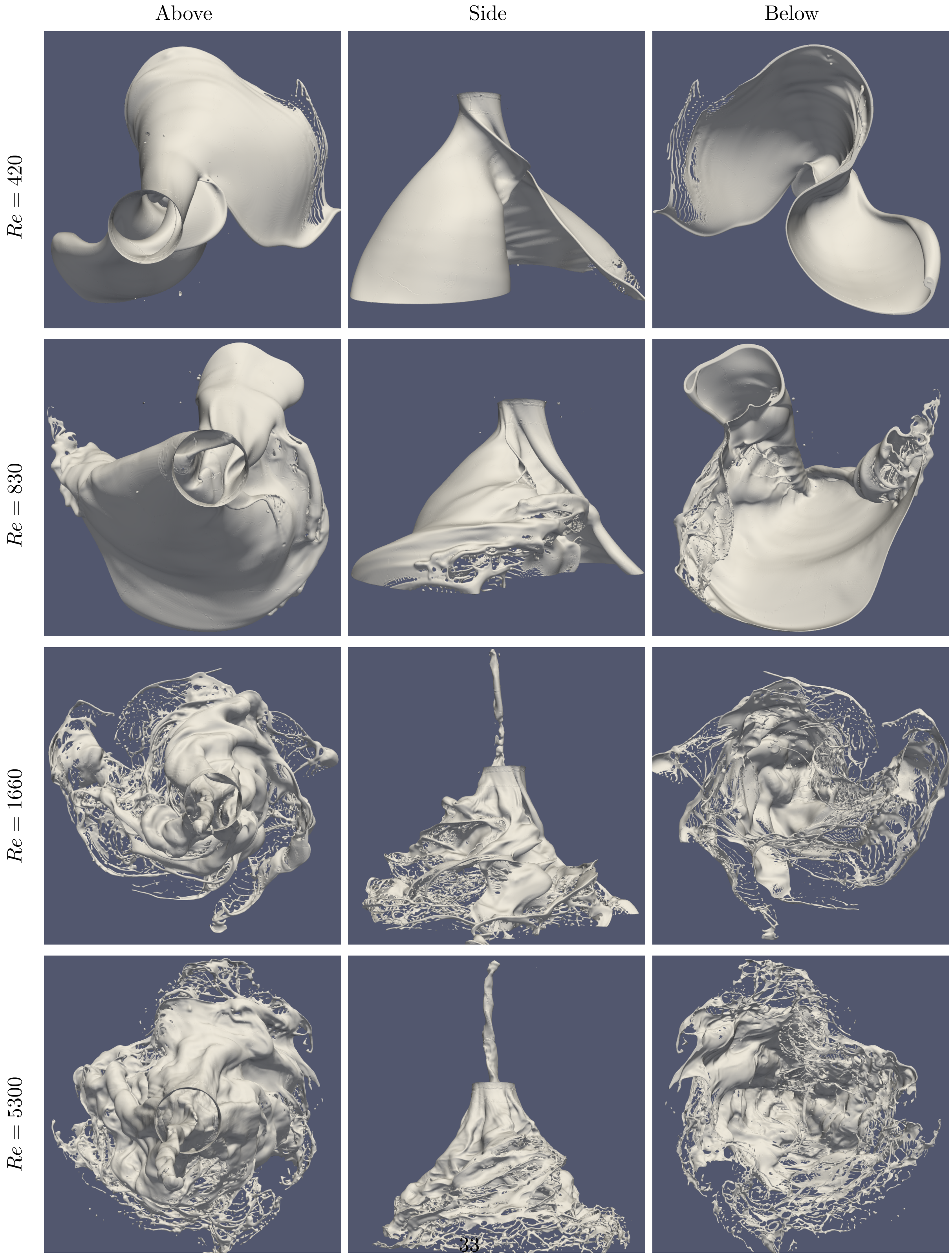

Figure 12: Near nozzle spray patterns at individual time instances: S-shaped spray ($Re = 420$), transitional spray of mixed type ($Re = 830$), and hollow cone spray with an air core ($Re \geq 1660$).

cases cover the transition from an S-shaped spray pattern at $Re = 420$ towards the hollow cone spray at $Re = 5300$.

At $Re = 420$ the discharge orifice is fully covered by liquid. The asymmetric velocity distribution at the orifice leads to an S-shaped liquid film emanating from the nozzle. The high viscosity of the liquid opposes the breakup of the sheet which does not greatly disintegrate in the domain under study. Somewhat similar twisting liquid films with two edges (S-shape) have been observed by Yao et al. (2012) with fluids of high viscosity in their measurements with a pulse operated pressure-swirl atomizer. In the present simulation the S-shaped film exhibits also a flapping motion analysed later on in the paper.

At $Re = 830$ the flow in the swirl chamber starts to exhibit a higher degree of fluctuations, although the air core is not yet formed. The liquid sheet remains largely intact in the refined simulation region but shows more irregular flapping motions. Breakup is initiated when the film grows thinner as a consequence of such a motion. At $Re = 830$, the spray pattern is best described as being in a transitional state between the S-shaped film and the hollow cone spray. At $Re \geq 1660$, the spray obtains its hollow cone shape. Disturbances and waves caused by the fluctuations of the velocity field are seen at the surface of the liquid sheet emanating from the nozzle. The film remains intact for a relatively short time after it exits the nozzle and before undergoing primary breakup into ligaments and small droplets.

As was discussed, in the lower Re cases the full hollow cone spray pattern is not yet formed. The classical description of transition towards the hollow cone spray undergoes the onion and tulip stages as depicted in Fig. 1c. The present simulations coincide with this picture only in the high Reynolds number range. This is attributed to the asymmetric inflow configuration in contrast to simplex nozzles. Here, high and low velocity regions are created in the velocity field at the orifice which directly lead to the formation of the S-shaped sheet at $Re = 420$. The in-plane components of the mean field in Fig. 10 show two velocity maxima which correspond to the two arcs seen in the film (see e.g. $Re = 420$ view from below in Fig. 12).

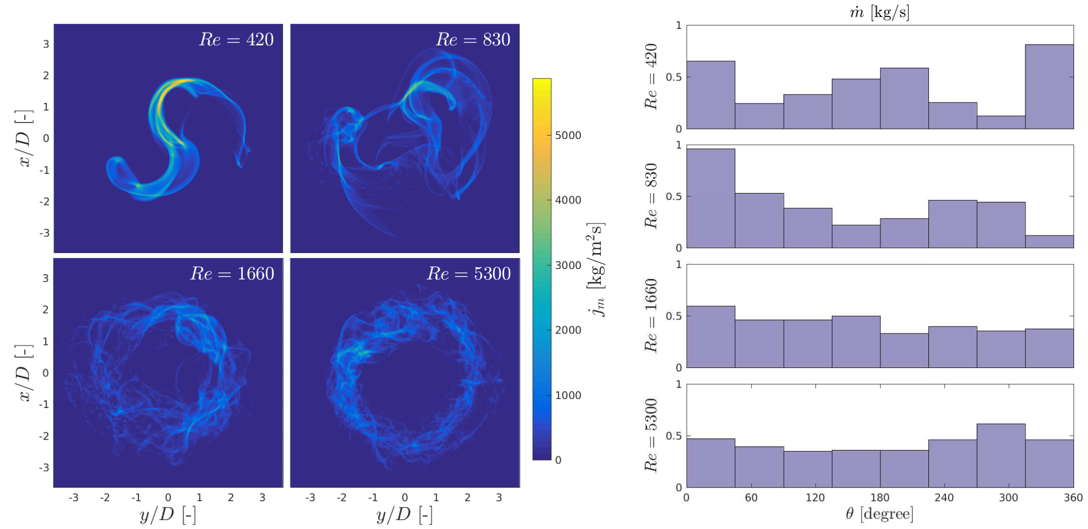

(a)

(b)

Figure 13: (a) Spatial distribution of the average mass flux, j_m, through a plane $2.7D$ downstream of the nozzle orifice. (b) Average mass flow through the plane divided into eight sectors. The sectors are defined according to the coordinate system and azimuthal angle depicted in Fig. 10.

3.3.2. Mass flow distribution

Typically simplex nozzles are tailored to produce a uniform mass distribution. However, as Fig. 11a showed, here the mass flux is not perfectly uniform for any of the considered Reynolds numbers. In Fig. 13 the averaged mass flux distribution is depicted at a plane located $2.7D$ downstream of the nozzle orifice. An ensemble average of time snapshots of the mass flux was used to calculate the average. It is clear from Fig. 13a that the S-shaped and transitional spray patterns of the two lower Re cases lead to more asymmetric mass flux distributions than for the higher Reynolds numbers. At $Re = 420$ the two preferred directions (positive and negative x-axis) are clearly visible in the histogram of Fig. 13b, whereas at higher Re, the distribution becomes more uniform as a function of the azimuthal angle.

3.3.3. Coherent motion of the film

Previously, a distinct fundamental frequency at $St = 0.82$ was observed at $Re = 420$ inside the swirl chamber. In contrast, such clear periodicity was not observed at higher Reynolds numbers. Next, we investigate how such inner-nozzle characteristics are transferred to the outer-nozzle liquid instability. Liquid film motion is visually characterized by the volume fraction field fluctuations (see e.g. Fig. 13a for average field). From such time snapshots it becomes clear that the S-shaped film flapping frequency is close to the $St = 0.82$ observed inside the swirl chamber. The objective of the following analysis is to use a modal decomposition technique to rigorously explore a potential link between the inner and outer-nozzle time frequencies.

As a modal decomposition technique we choose the principal component analysis (PCA). The analysis is analogous to the proper orthogonal decomposition (POD) which is typically used to find and extract energetic coherent structures from complex turbulent/transitional velocity fields (Berkooz et al., 1993; Chatterjee, 2000; Borée, 2003). In contrast to finding kinetic energy containing modes, here PCA is used to analyse the spatio-temporal motion of the volume fraction field. It is important to note that the following analysis does not offer information on the energy containing flow structures. Instead the analysis aims at providing information on the position of the fluctuating liquid-gas boundary.

Next, the theory of the PCA is briefly introduced following the discussion in (Vuorinen et al., 2013) and (Kahila et al., 2017). The aim is to decompose the volume fraction field into orthogonal spatial modes, i.e. the field is projected onto an orthogonal function basis. Here, the method of snapshots by Sirovich (1987) is applied. The analysis is carried out for a series of snapshots which are 2d cross-sections of the 3d volume fraction field (see Fig. 14a). The algorithm consists of the following steps. First, the mean values are subtracted from the snapshots and the fluctuating part of the 2d field data is assembled into vectors $\alpha_k = \alpha(t_k)$, $k = 1, ..., N$, where N is the number of time snapshots. After this, the individual vectors are collected as the columns of the snapshot matrix

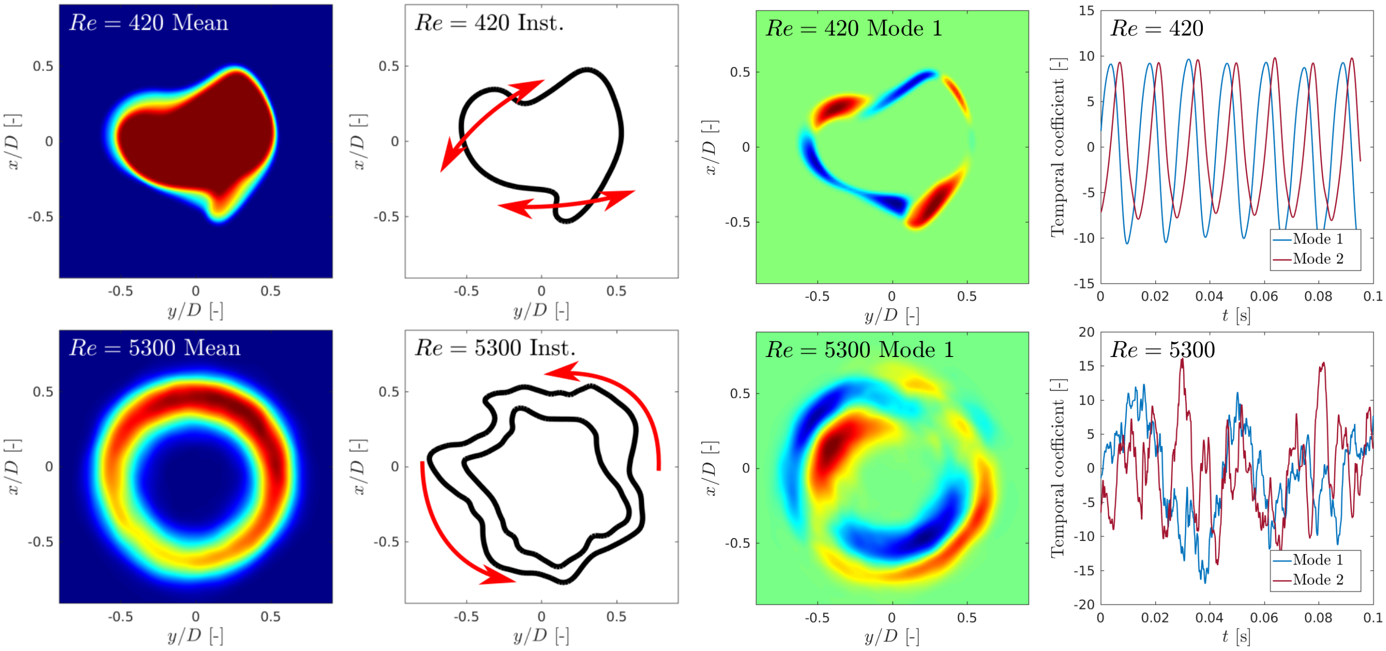

(a) (b)

Figure 14: PCA of the volume fraction field at $Re = 420$ and 5300. The plane under study is located at $0.45D$ from the orifice. (a) The mean and an instantaneous volume fraction field. The arrows indicate the direction of the movement of disturbances. (b) The first spatial mode and the temporal coefficients of the two first modes.

M. The eigenvalue analysis of the covariance matrix $C = M^T M$ allows the construction of an orthogonal basis of K modes $\psi_i = M v_i$, $i = 1, ..., K$ arranged in the decreasing order of eigenvalues of C such that $\lambda_1 \geq \lambda_2 \geq ... \geq \lambda_K \geq 0$. Above, v_i is the i-th eigenvector of C. Any snapshot can then be expressed as a sum

$$\alpha_k = \sum_{i=1}^{K} a_i(t_k)\psi_i, \tag{13}$$

where the temporal coefficients $a_i(t_k)$ are computed as inner products (projections) between the snapshot and the basis function. The analysis was carried out at a plane located $0.45D$ downstream from the nozzle orifice. Some example modes and time coefficients are depicted in Fig. 14 for $Re = 420$ and 5300.

At $Re = 420$, the liquid evolves in S-shaped cross-sectional pattern which is clearly seen after about $1.5D$ from the nozzle orifice (see Fig. 12). Here, the PCA analysis is carried out for data taken $0.45D$ from the exit where the liquid has not yet reached the S-shape (see Fig. 14a). The periodic flapping motion near the orifice is indicated by the arrows in Fig. 14a. The PCA reveals several coupled mode pairs: modes 1 and 2 (73 ± 6 Hz), 3 and 4 (140 ± 9 Hz), 5 and 6 (210 ± 5 Hz), and 7 and 8 (284 ± 5 Hz) form pairs characterized by their shared oscillation frequency and spatial size (see e.g. (Vuorinen et al., 2013)). Above, the frequencies have been determined from the power spectra of the temporal coefficients. The first mode is illustrated in Fig. 14b together with the temporal coefficients of the two first modes. By comparing the frequencies to the oscillation frequency exhibited inside the swirl chamber (see Fig. 8), it is evident that the same fundamental frequency at $St = 0.82$ is observed together with its higher harmonics. The observations indicate a clear link between the periodic velocity field fluctuation inside the swirl chamber and the flapping motion of the liquid film in the nozzle near field at $Re = 420$.

At $Re = 5300$, the motion of the liquid film is more irregular as is visualized by the instantaneous snapshot of the film in Fig. 14a. The film shows perturbations both in its thickness and location and the disturbances travel in the swirling direction of the flow indicated by the arrows. Although spatial modes can be discerned in the PCA results, the temporal coefficients contain energy on a range of frequencies and do not allow to draw definite conclusions on coherent structures of the film (see Fig. 14a). This is somewhat expected as also the velocity fluctuations show continuous spectra at high Re (Fig. 8b) indicating the presence of a range of frequencies.

3.3.4. Breakup process of hollow cone sprays

Several mechanisms may affect the breakup process of the conical film. First, the liquid film thickness, inertia and turbulence at the orifice affect the sheet instability. Second, viscous effects resist the breakup and smoothen the velocity distribution inside the film. Third, the radial outward motion of the swirl causes

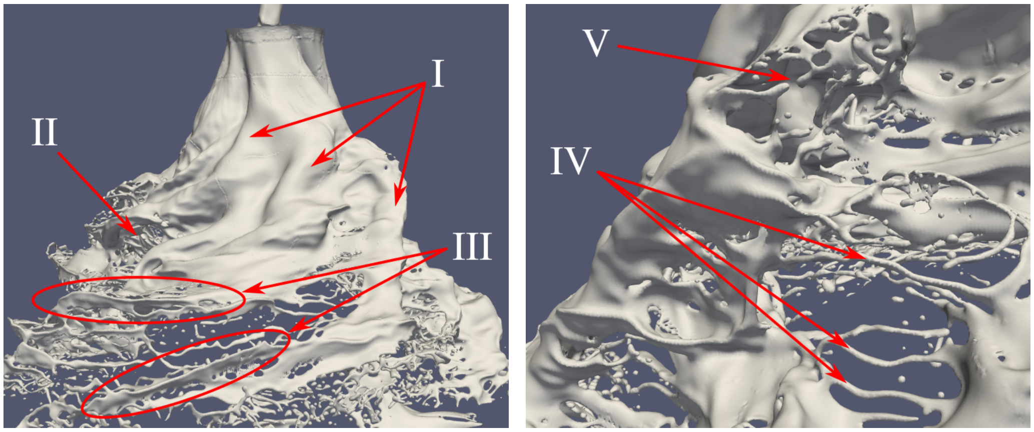

Figure 15: Structures observed in the breakup of the film at $Re = 5300$. Disturbance waves (I), breakup of the film between two wave crests (II), large (III) and small (IV) length scale ligaments, and breakup of ligaments by pinching (V).

the film to become thinner as it moves further from the discharge orifice. As a last remark, aerodynamic forces from the interaction with the surrounding gas promote the breakup of the liquid film. As shown in Fig. 12, the breakup process is highly complex and cannot be attributed to a single breakup mechanism alone. Next, we concentrate on the $Re = 5300$ case and observe features that result from the different mechanisms affecting the atomization process.

Some key features observed during the initial breakup are summarized in Fig. 15. The fluctuating velocity field at the orifice is manifested as wave-like perturbations of the liquid film (I). The perturbations are exhibited immediately after the liquid exits the nozzle. Similar structures have been observed by Shao et al. (2017) in their simulations of swirling atomization from an annular pipe with turbulent inlet conditions. These disturbances travel further downstream and grow. The growth forces the film to thin and when the film is thin enough breakup is observed (II in Fig. 15 and I in Fig. 16). The breakup typically occurs first between two wave crests. Both larger (III) and smaller (IV) scale ligaments are generated. The large-scale ligaments are formed at the positions of the wave crests as a result of the film disintegrating around the crest. The small-scale

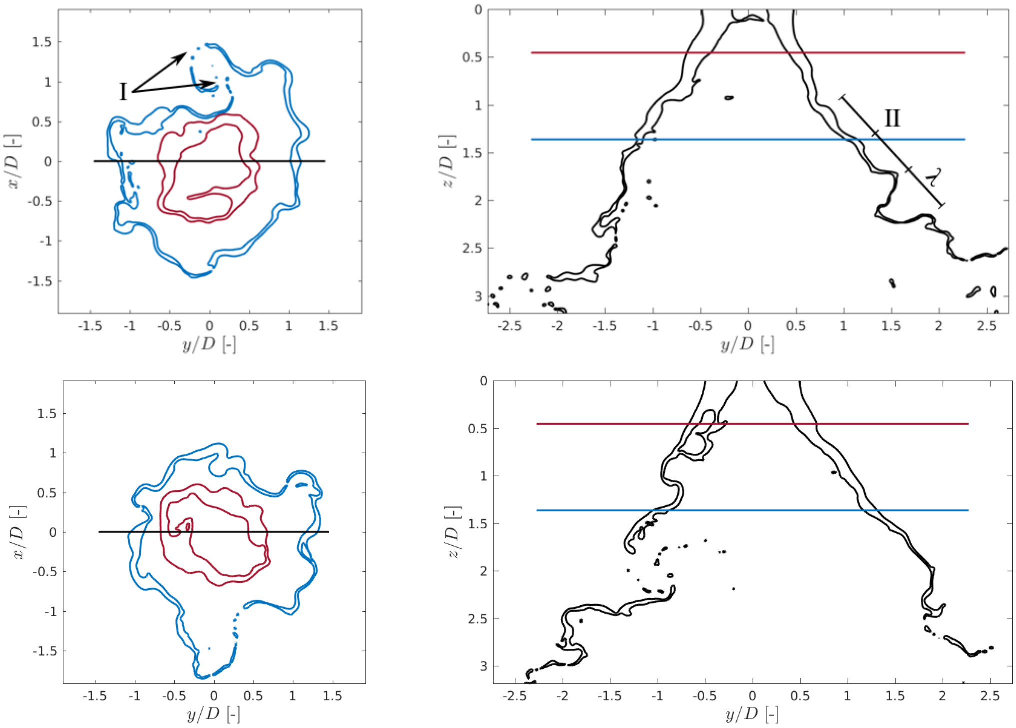

Figure 16: The location of the film at two different time instances (upper and lower rows) in the $Re = 5300$ case. The colored lines show the locations of the cross-sections of the corresponding color.

ligaments are generated together with droplets as the film grows thinner and disintegrates. Such small-scale structures have been previously observed, for example, in the DNS study of Galbiati et al. (2016c). Here, the subsequent pinching of the small-scale ligaments into shorter ligaments and droplets can also be observed (V). The scale separation between the nozzle diameter and the smallest droplets is very large. In the present LES, the coherent structures (I in Fig. 15) are captured rather well. However, the subsequent ligament formation is only qualitatively captured as the ligament thickness is solved typically by ∼4–8 cells (e.g. IV in Fig. 15).

Fig. 16 illustrates the film position at two time instances. Wave-like struc-

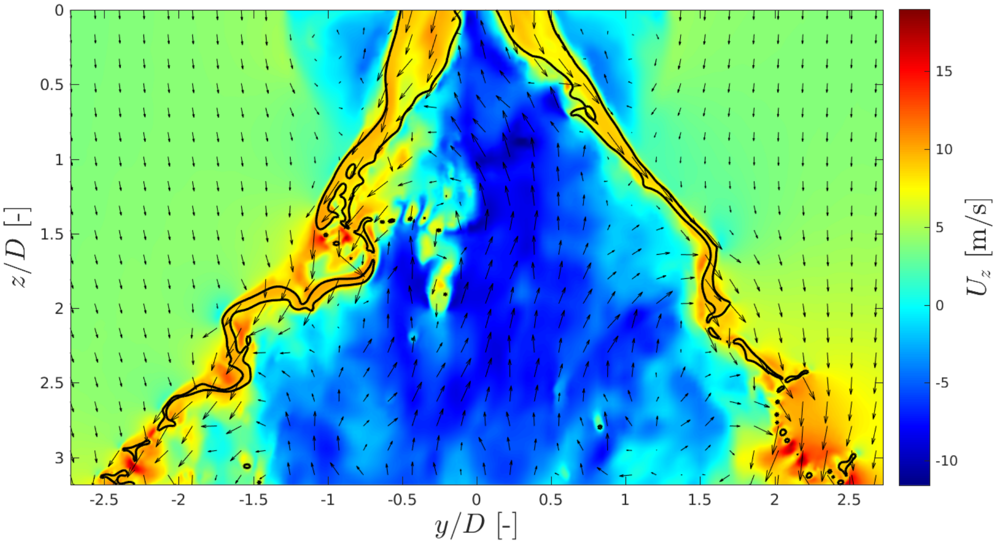

Figure 17: Instantaneous velocity field (vectors) and the z-component of the velocity (color) at a plane intersecting the discharge orifice at $Re = 5300$. The gas-liquid interface is indicated with the black line.

tures and abrupt variations are visible both in the film thickness and location. Although the large initial disturbances from the orifice make the observation of pure aerodynamic instabilities challenging, instability modes typical to liquid film breakup are visible occasionally. Fig. 16 provides qualitative evidence of a sinusoidal instability of the film (II) which is a typical instability mode of liquid sheets (Ashgriz, 2011). Similar instabilities have been observed also in DNS of conical swirled jets by Galbiati et al. (2016c). We also note that a recirculation zone is present at the center of the spray as depicted in Fig. 17. The observation agrees with the study of Shao et al. (2017) who noted a similar feature. The reverse flow inside the zone may have a destabilizing effect on the film because of the increased velocity gradients compared to a stagnant spray center.

Large-scale ligaments are generated at the locations of the wave crests while small-scale ligaments and droplets are also created in the process. Based on estimates on the present numerical results, we note that the typical Weber numbers of the droplets are in the stable regime. The droplet diameter corresponding to the critical Weber number of $We_{crit} = 11$ can be estimated to be $d_{crit} = We_{crit}\sigma/U_{rel}^2\rho_g \approx 1.9$ mm (Ashgriz, 2011). Here, a conservative estimate of $U_{rel} = 20$ m/s was used for the relative velocity. In comparison to the critical diameter, the numerical results indicate smaller typical diameters in the range of 0.5–1.0 mm. Additionally, the observed ligament diameters suggest that surface tension effects are important also for the ligament evolution. Typically, ligaments breakup into droplets through the Rayleigh-Plateau instability mechanism. Although such events are observed in the simulation (e.g. V in Fig. 15), the majority of the ligaments leave the refined simulation domain before undergoing further breakup.

4. Conclusions

In this work, a large-scale pressure-swirl atomizer was studied by large-eddy simulation. The current nozzle geometry differs greatly from the typical simplex atomizer, which most of the previous work on pressure-swirl atomizers has concentrated on. The focus of this study was on assessing and quantifying the performance of the atomizer when operated with high viscosity fluids. The Reynolds number effects were studied by conducting a sweep with varying viscosity. The implications on the flow field inside the nozzle as well as the spray in the nozzle near field were studied. The sweep covers a range of conditions where the near field spray develops from an asymmetric liquid film to a hollow cone spray.

Some of the main findings of the study can be summarized as follows:

1. At $Re \leq 830$, the flow inside the nozzle is laminar and neither an air core or a hollow cone spray is present. At $Re \geq 1660$, an air core is formed resulting in a hollow cone spray.
2. The near field spray patterns of onion and tulip shapes are characteristic for simplex atomizers. However, such shapes were not observed in the present simulations, and instead, an S-shaped liquid film spray was formed

at $Re = 420$. The present numerical results indicate that this may be caused by the non-uniform velocity distribution at the outlet orifice.

3. The air core and therefore the film thickness at the discharge orifice was observed to fluctuate significantly. The film thickness was 8.5 mm at $Re = 1660$ and 7.6 mm at $Re = 5300$, while the standard deviations of the thicknesses were 25% and 18%, respectively. The fluctuations may be explained by the helical structure of the air core inside the swirl chamber.
4. At $Re = 420$ a periodic flapping of the liquid sheet in the nozzle near field was observed. It was hypothesized that the flapping may be caused by a vortex shedding mechanism inside the swirl chamber where a similar periodic variation in the velocity field was noted. The frequency of the periodic movement was measured to be $f = 73 \pm 6$ Hz.
5. The initial breakup of the intact liquid sheet is affected by four mechanisms: (a) disturbances caused by the fluctuating velocity field and film thickness at the discharge orifice, (b) aerodynamic forces from the surrounding gas and particularly the recirculation zone inside the hollow cone spray, (c) the radial outward motion which causes the film to thin down, as well as, (d) the viscous effects which resist the breakup by stabilizing the film.
6. The uniformity of the mass flow distribution was quantified in the nozzle near field and it was concluded that increasing the Reynolds number led to a more uniform distribution.
7. The unsteady effects of the nozzle inner flow were noted to cause significant fluctuations to the near nozzle liquid sheet which advocates a simulation strategy solving both the inner and external nozzle flow in the same simulation.

Acknowledgements

The first author gratefully acknowledges the financial support from the Doctoral Programme of Aalto University School of Engineering. The computational resources for this study were provided by CSC - Finnish IT Center for Science.

References

Amini, G., 2016. Liquid flow in a simplex swirl nozzle. International Journal of Multiphase Flow 79, 225 – 235. doi:`10.1016/j.ijmultiphaseflow.2015.09.004`.

Ashgriz, N., 2011. Handbook of Atomization and Sprays: Theory and Applications. Springer US. doi:`10.1007/978-1-4419-7264-4`.

Aspden, A., Nikiforakis, N., Dalziel, S., Bell, J., 2008. Analysis of implicit les methods. Communications in Applied Mathematics and Computational Science 3, 103 – 126. doi:`10.2140/camcos.2008.3.103`.

Berkooz, G., Holmes, P., Lumley, J.L., 1993. The proper orthogonal decomposition in the analysis of turbulent flows. Annual Review of Fluid Mechanics 25, 539–575. doi:`10.1146/annurev.fl.25.010193.002543`.

Binnie, A.M., Harris, D.P., 1950. The application of boundary-layer theory to swirling liquid flow through a nozzle. The Quarterly Journal of Mechanics and Applied Mathematics 3, 89 – 106. doi:`10.1093/qjmam/3.1.89`.

Borée, J., 2003. Extended proper orthogonal decomposition: a tool to analyse correlated events in turbulent flows. Experiments in Fluids 35, 188–192. doi:`10.1007/s00348-003-0656-3`.

Boris, J., Grinstein, F., Oran, E., Kolbe, R., 1992. New insights into large eddy simulation. Fluid Dynamics Research 10, 199 – 228. doi:`10.1016/0169-5983(92)90023-P`.

Brackbill, J., Kothe, D., Zemach, C., 1992. A continuum method for modeling surface tension. Journal of Computational Physics 100, 335 – 354. doi:`10.1016/0021-9991(92)90240-Y`.

Chatterjee, A., 2000. An introduction to the proper orthogonal decomposition. Current Science 78, 808–817.

Chinn, J.J., 2008. The numerics of the swirl atomizer, in: ILASS-Europe 2008 - 22th Conference on Liquid Atomization and Spray Systems.

Cooper, D., Yule, A.J., 2001. Waves on the air core / liquid interface of a pressure swirl atomizer, in: ILASS-Europe 2001 - 17th Conference on Liquid Atomization and Spray Systems.

Dash, S.K., Halder, M.R., Peric, M., Som, S.K., 2001. Formation of air core in nozzles with tangential entry. Journal of Fluids Engineering 123, 829 – 835. doi:`10.1115/1.1412845`.

Deshpande, S.S., Anumolu, L., Trujillo, M.F., 2012. Evaluating the performance of the two-phase flow solver interfoam. Computational Science & Discovery 5, 014016.

Desjardins, O., Pitsch, H., 2010. Detailed numerical investigation of turbulent atomization of liquid jets. Atomization and Sprays 20, 311 – 336.

Ding, J.W., Li, G.X., Yu, Y.S., Li, H.M., 2016. Numerical investigation on primary atomization mechanism of hollow cone swirling sprays. Journal of Engineering for Gas Turbines and Power 2016. doi:`10.1155/2016/1201497`.

Donjat, D., Estivalezes, J.L., Michau, M., 2002. A description of the pressure swirl atomizer internal flow, in: ASME 2002 Fluids Engineering Division Summer Meeting.

El Khoury, G.K., Schlatter, P., Noorani, A., Fischer, P.F., Brethouwer, G., Johansson, A.V., 2013. Direct numerical simulation of turbulent pipe flow at moderately high reynolds numbers. Flow, Turbulence and Combustion 91, 475 – 495. doi:`10.1007/s10494-013-9482-8`.

Fu, Q.f., 2016. Numerical simulation of the internal flow of swirl atomizer under ambient pressure. Proceedings of the Institution of Mechanical Engineers, Part C: Journal of Mechanical Engineering Science 230, 2650 – 2659. doi:10.1177/0954406215598803.

Fureby, C., Grinstein, F.F., 1999. Monotonically integrated large eddy simulation of free shear flows. AIAA Journal 37, 544 – 556. doi:10.2514/2.772.

Fureby, C., Grinstein, F.F., 2002. Large eddy simulation of high-reynolds-number free and wall-bounded flows. Journal of Computational Physics 181, 68 – 97. doi:10.1006/jcph.2002.7119.

Fuster, D., Bagué, A., Boeck, T., Moyne, L.L., Leboissetier, A., Popinet, S., Ray, P., Scardovelli, R., Zaleski, S., 2009. Simulation of primary atomization with an octree adaptive mesh refinement and vof method. International Journal of Multiphase Flow 35, 550 – 565. doi:10.1016/j.ijmultiphaseflow.2009.02.014.

Galbiati, C., Ertl, M., Tonini, S., Cossali, G.E., Weigand, B., 2016a. DNS Investigation of the Primary Breakup in a Conical Swirled Jet. Springer International Publishing, Cham. pp. 333 – 347. doi:10.1007/978-3-319-24633-8_22.

Galbiati, C., Tonini, S., Conti, P., Cossali, G.E., 2016b. Numerical simulations of internal flow in an aircraft engine pressure swirl atomizer. Journal of Propulsion and Power 32, 1433 – 1441. doi:10.2514/1.B35944.

Galbiati, C., Tonini, S., Weigand, B., Cossali, G.E., 2016c. Direct numerical simulation of primary break-up in swirling liquid jets, in: ICMF-2016 - 9th International Conference on Multiphase Flow.

Grinstein, F.F., Fureby, C., 2007. On flux-limiting-based implicit large eddy simulation. Journal of Fluids Engineering 129, 1483 – 1492. doi:10.1115/1.2801684.

Herrmann, M., 2010. Detailed numerical simulations of the primary atomization of a turbulent liquid jet in crossflow. Journal of Engineering for Gas Turbines and Power 131. doi:http://dx.doi.org/10.1115/1.4000148.

Hirt, C., Nichols, B., 1981. Volume of fluid (vof) method for the dynamics of free boundaries. Journal of Computational Physics 39, 201 – 225. doi:`10.1016/0021-9991(81)90145-5`.

Ito, H., 1987. Flow in curved pipes. JSME international journal 30, 543 – 552. doi:`10.1299/jsme1987.30.543`.

Jasak, H., 2009. Openfoam: Open source cfd in research and industry. International Journal of Naval Architecture and Ocean Engineering 1, 89 – 94. doi:`10.2478/IJNAOE-2013-0011`.

Jasak, H., Weller, H., Gosman, A., 1999. High resolution nvd differencing scheme for arbitrarily unstructured meshes. International Journal for Numerical Methods in Fluids 31, 431 – 449. doi:`10.1002/(SICI)1097-0363(19990930)31:2<431::AID-FLD884>3.0.CO;2-T`.

Kahila, H., Kaario, O., Wehrfritz, A., Vuorinen, V., 2017. Proper orthogonal decomposition analysis of the engine combustion network spray a, in: ILASS-Americas 29th Annual Conference on Liquid Atomization and Spray Systems.

Kahila, H., Wehrfritz, A., Kaario, O., Masouleh, M.G., Maes, N., Somers, B., Vuorinen, V., 2018. Large-eddy simulation on the influence of injection pressure in reacting spray a. Combustion and Flame 191, 142 – 159. doi:`10.1016/j.combustflame.2018.01.004`.

Keskinen, J.P., Vuorinen, V., Kaario, O., Larmi, M., 2016. Influence of mesh deformation on the quality of large eddy simulations. International Journal for Numerical Methods in Fluids 82, 171 – 197. doi:`10.1002/fld.4215`.

Kim, S., Khil, T., Kim, D., Yoon, Y., 2009. Effect of geometric parameters on the liquid film thickness and air core formation in a swirl injector. Measurement Science and Technology 20, 015403.

Lefebvre, A., 1989. Atomization and Sprays. First edition ed., CRC Press, Boca Raton.

Li, X., Gao, H., Soteriou, M.C., 2017. Investigation of the impact of high liquid viscosity on jet atomization in crossflow via high-fidelity simulations. Physics of Fluids 29, 082103. doi:`10.1063/1.4996178`.

Maly, M., Jedelsky, J., Slama, J., Janackova, L., Sapik, M., Wigley, G., Jicha, M., 2018. Internal flow and air core dynamics in simplex and spill-return pressure-swirl atomizers. International Journal of Heat and Mass Transfer 123, 805 – 814. doi:`10.1016/j.ijheatmasstransfer.2018.02.090`.

Margolin, L.G., Rider, W.J., Grinstein, F.F., 2006. Modeling turbulent flow with implicit les. Journal of Turbulence 7, 1 – 27. doi:`10.1080/14685240500331595`.

Meredith, K., Zhou, X., Wang, Y., 2017. Towards resolving the atomization process of an idealized fire sprinkler with vof modeling, in: ILASS-Europe 2017 - 28th Conference on Liquid Atomization and Spray Systems. doi:`http://dx.doi.org/10.4995/ILASS2017.2017.5014`.

Ponstein, J., 1959. Instability of rotating cylindrical jets. Applied Scientific Research, Section A 8, 425 – 456. doi:`10.1007/BF00411768`.

Renze, P., Heinen, K., Schönherr, M., 2011. Experimental and numerical investigation of pressure swirl atomizers. Chemical Engineering & Technology 34, 1191 – 1198. doi:`10.1002/ceat.201100054`.

Rizk, N.K., Lefebvre, A.H., 1985. Internal flow characteristics of simplex swirl atomizers. Journal of Propulsion and Power 1, 193 – 199. doi:`10.2514/3.22780`.

Roenby, J., Bredmose, H., Jasak, H., 2016. A computational method for sharp interface advection. Royal Society Open Science 3. doi:`10.1098/rsos.160405`.

Saha, A., Lee, J.D., Basu, S., Kumar, R., 2012. Breakup and coalescence characteristics of a hollow cone swirling spray. Physics of Fluids 24, 124103. doi:`10.1063/1.4773065`.

Salvador, F., Ruiz, S., Crialesi-Esposito, M., Blanquer, I., 2018. Analysis on the effects of turbulent inflow conditions on spray primary atomization in the near-field by direct numerical simulation. International Journal of Multiphase Flow 102, 49 – 63. doi:`10.1016/j.ijmultiphaseflow.2018.01.019`.

Senecal, P., Schmidt, D., Nouar, I., Rutland, C., Reitz, R., Corradini, M., 1999. Modeling high-speed viscous liquid sheet atomization. International Journal of Multiphase Flow 25, 1073 – 1097. doi:`10.1016/S0301-9322(99)00057-9`.

Shao, C., Luo, K., Yang, Y., Fan, J., 2017. Detailed numerical simulation of swirling primary atomization using a mass conservative level set method. International Journal of Multiphase Flow 89, 57 – 68. doi:`10.1016/j.ijmultiphaseflow.2016.10.010`.

Shinjo, J., Umemura, A., 2011. Surface instability and primary atomization characteristics of straight liquid jet sprays. International Journal of Multiphase Flow 37, 1294 – 1304. doi:`10.1016/j.ijmultiphaseflow.2011.08.002`.

Sirovich, L., 1987. Turbulence and the dynamics of coherent structures part i: Coherent structures. Quarterly of Applied Mathematics 45, 561–571.

Som, S.K., 2012. Air core in pressure swirl atomizing nozzles. Atomization and sprays 22, 283 – 303.

Suyari, M., Lefebvre, A.H., 1986. Film thickness measurements in a simplex swirl atomizer. Journal of Propulsion and Power 2, 528 – 533.

Vuorinen, V., Yu, J., Tirunagari, S., Kaario, O., Larmi, M., Duwig, C., Boersma, B., 2013. Large-eddy simulation of highly underexpanded transient gas jets. Physics of Fluids 25, 016101. doi:`10.1063/1.4772192`.

Wehrfritz, A., Kaario, O., Vuorinen, V., Somers, B., 2016. Large eddy simulation of n-dodecane spray flames using flamelet generated manifolds. Combustion and Flame 167, 113 – 131. doi:`10.1016/j.combustflame.2016.02.019`.

White, F.M., 2006. Viscous fluid flow. Third international ed., McGraw-Hill.

Wimmer, E., Brenn, G., 2013. Viscous flow through the swirl chamber of a pressure-swirl atomizer. International Journal of Multiphase Flow 53, 100 – 113. doi:`10.1016/j.ijmultiphaseflow.2013.02.003`.

Xia, H., Tucker, P.G., 2012. Numerical simulation of single-stream jets from a serrated nozzle. Flow, Turbulence and Combustion 88, 3 – 18. doi:`10.1007/s10494-011-9377-5`.

Yang, X., Turan, A., 2017. Simulation of liquid jet atomization coupled with forced perturbation. Physics of Fluids 29, 022103. doi:`10.1063/1.4976621`.

Yao, S., Zhang, J., Fang, T., 2012. Effect of viscosities on structure and instability of sprays from a swirl atomizer. Experimental Thermal and Fluid Science 39, 158 – 166. doi:`10.1016/j.expthermflusci.2012.01.020`.